



30 Nonlinear, low-frequency wave excitation leads to surge and pitch resonance motion of the structure, causing high  
31 loads. The underprediction of the low-frequency response can therefore be attributed to an underprediction of the  
32 nonlinear wave excitation and/or overprediction of the hydrodynamic damping at the surge and pitch resonance  
33 frequencies.

34 Extensive study of the low-frequency responses of floating wind semisubmersibles has been carried out. The  
35 experimental investigation by do Carmo et al. [2] investigated the forced-oscillation, free-decay, and slow-drift  
36 motions of a semisubmersible offshore wind platform. The calm-water free-decay experiments and forced-  
37 oscillation experiments led to different surge damping values, with those from forced oscillation being consistently  
38 lower; however, even with the lower damping coefficient from forced oscillation, the potential-flow model still  
39 underpredicted the slow-drift motion, corroborating the trend identified in OC5 [1]. This observation also suggests  
40 that the underprediction of low-frequency wave excitation must play a role in the overall underprediction of the  
41 response, at least in surge. The substantial underprediction of the nonlinear, difference-frequency surge force on  
42 another offshore wind semisubmersible by full second-order potential-flow quadratic transfer functions (QTFs) was  
43 confirmed in an experimental campaign with a fixed model in bichromatic waves by Lopez-Pavon et al. [3], even  
44 with the wave amplitudes deliberately kept low to reduce viscous effects. This underprediction of the low-frequency  
45 response has also been observed by many other researchers [4,5].

46 To better understand and address this underprediction, Phase I of the present OC6 (OC5 with unCertainty)  
47 project organized a three-way validation study into the low-frequency responses of the OC6-DeepCwind  
48 semisubmersible with new wave-basin experiments [6–8] and numerical investigations with both mid-fidelity  
49 engineering tools [9] and high-fidelity computational fluid dynamics (CFD) simulations [10–12]. The experimental  
50 setups with the OC6-DeepCwind semisubmersible are shown in Figure 1. With the fixed configuration (Figure 1a),  
51 the floater was restrained, and the wave loads on the structure were measured. With the floating configuration in  
52 Figure 1b, the wave-induced motion of the floater was measured instead. The tools used in the study of [9] include a  
53 range of mid-fidelity models based on the Morison equation with a strip-theory formulation, potential-flow  
54 solutions, or a combination of both, such as the OpenFAST model developed by the National Renewable Energy  
55 Laboratory (NREL). The NREL OpenFAST tool models the floater in the time domain and incorporates both the  
56 first- and second-order frequency-domain potential-flow solutions to model the wave excitation and radiation loads.  
57 In addition to a global linear damping matrix, the OpenFAST model also evaluates quadratic drag forces based on

58 empirical drag coefficients to model the viscous effects. Distributed transverse drag is evaluated along the various  
59 members of the floater following a strip-theory-type formulation, and lumped drag forces in the normal directions  
60 are also evaluated on the faces of the heave plates. The collaborative study of [9] with the engineering models,  
61 which involved more than two dozen organizations submitting results from different state-of-the-art tools, showed  
62 again that all models underpredicted, to varying degrees, both the low-frequency wave excitation on a fixed  
63 structure and the motion of a freely floating structure. The CFD simulations, on the other hand, tend to provide  
64 better predictions of the low-frequency wave excitation when compared to the experiment [12], suggesting CFD  
65 results can be used to further study the underprediction issue and provide reference data for tuning the engineering  
66 models in lieu of, or in addition to, the wave-basin experiments.

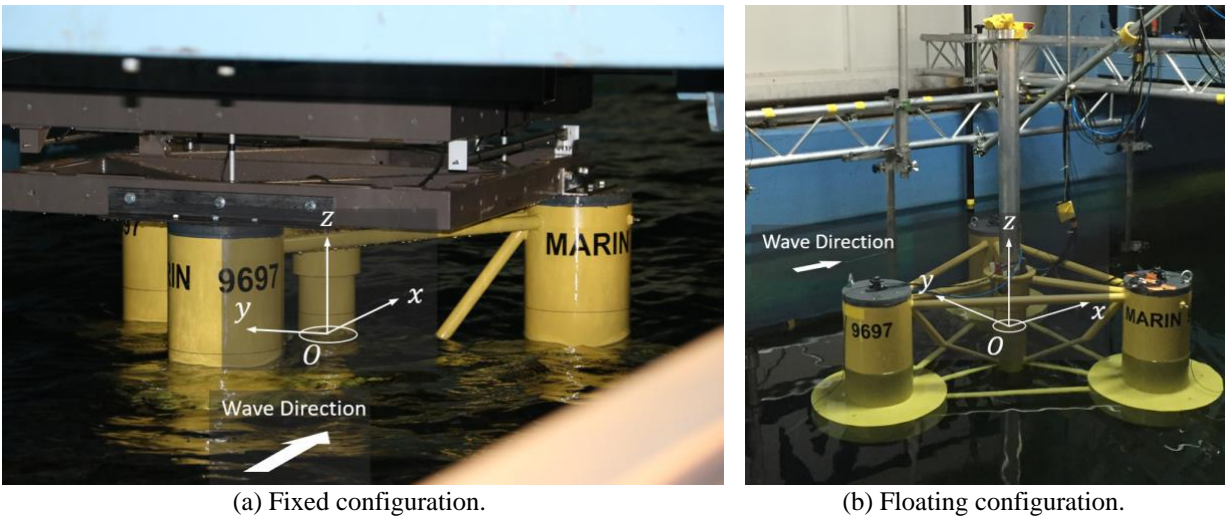


**Figure 1.** Setups of (a) the fixed configuration and (b) the freely floating configuration of the DeepCwind floating wind semisubmersible of the OC6 Phase Ia model experiment campaign at the concept basin of the Maritime Research Institute Netherlands (MARIN). Photo by Amy Robertson, NREL.

67 At the low surge and pitch resonance frequencies, viscous damping generally dominates over wave radiation  
68 damping [13]; therefore, most effort to address the underprediction of low-frequency responses has focused on  
69 improving the tuning of the viscous drag coefficients used by the models. In the OC6 Phase I investigation with  
70 engineering models [9], a consistent trend was observed in which higher transverse Morison drag coefficients  
71 increased the predicted low-frequency surge force on a fixed floater, leading to better agreement with the  
72 experiment. The free-decay motion of the structure was also better predicted; however, the increased drag also  
73 decreased the motion response of the system under irregular wave excitation, exacerbating the underprediction. The  
74 same observation was also made by Lemmer et al. [14], who showed that the best drag coefficient for free-decay

75 motion was 3 to 5 times that for wave conditions. This conflict can be resolved with the help of a depth-dependent  
76 transverse drag coefficient [15–17], which is further explored in the present study. Böhm et al. [18] systematically  
77 tuned the transverse drag coefficient for the columns and the axial/normal drag coefficient for the heave plates for an  
78 OpenFAST model of the OC6-DeepCwind semisubmersible using a global pattern search algorithm. A single heave-  
79 plate axial drag coefficient was used, which simultaneously affected the heave and pitch responses of the structure.  
80 The outcome of the optimization clearly indicated that no single value of the heave-plate drag coefficient can  
81 provide acceptable predictions for both heave and pitch motions. It was conjectured that the existing OpenFAST  
82 model was unable to represent pitch damping well. With two separate optimization searches, one based on surge and  
83 heave motion and the other on pitch motion only, the results showed that the axial drag coefficient for the heave  
84 plates that worked best for heave motion was approximately double that for pitch, rendering a compromise  
85 impossible. Lemmer et al. [14] argued that heave motion is less important for floating wind turbines and tuned the  
86 axial drag coefficients of the heave plates based on pitch motion only. In general, it is possible to obtain good  
87 agreement between the model and the experiment for selected low-frequency responses by specifically tuning the  
88 drag coefficients against them as demonstrated by Simos et al. [19] and Pegalajar-Jurado and Bredmose [20] with  
89 the slow drift motion, but it is challenging to simultaneously obtain satisfactory predictions of all low-frequency  
90 response metrics of interest with the same set of model coefficients, even just for a single wave condition. To  
91 achieve this, some modifications to the modeling practice and model formulation are required. One notable approach  
92 aimed at improving the predictions of low-frequency wave excitation and floater response is the QTF-correction  
93 method of Li and Bachynski-Polić [21]. With this method, the difference-frequency QTFs for the wave excitation on  
94 a fixed structure from second-order potential-flow theory are modified and scaled up based on the results from a  
95 series of CFD simulations with bichromatic-incident waves. The modified QTFs are subsequently used as inputs to a  
96 mid-fidelity engineering model, improving the predictions of the nonlinear, low-frequency wave loads on a fixed  
97 structure [21]. Subsequent application of the modified QTFs in the modeling of the same structure under a floating  
98 condition also led to improved predictions of the low-frequency resonance motion [22].

99 In this article, we propose a different approach to address the underprediction of the nonlinear, low-frequency  
100 wave loads and responses by mid-fidelity tools. Instead of modifying the QTFs, we devised three modifications to  
101 the empirical drag forces in the existing OpenFAST model developed by NREL for the OC5/6 projects [9]. The  
102 modifications are inspired by the data and observations gathered throughout the OC6 Phase I project. Although there

103 are potentially many possible approaches to obtain improved low-frequency predictions, at least for a given wave  
104 condition and geometry, we strived to formulate modifications that are physically justifiable and general without  
105 substantially increasing the difficulty of model tuning. Note that we primarily focused on the responses of the  
106 structure in waves. The behaviors of the structure in calm water, such as free decay and forced oscillation, were not  
107 explicitly considered; however, we kept the model coefficients from our original OpenFAST model [9], which were  
108 tuned against free-decay motion [18], to retain the calm-water characteristics of the model as much as possible. The  
109 improved model described here is one of the principal outcomes of the OC6 Phase I project.

110 The physical problem investigated in this article is described in Section 2. The original OpenFAST model  
111 developed for OC5/6 by NREL [9] is described in detail in Section 3 for reference and to illustrate the  
112 underprediction of low-frequency wave loads and motion response encountered in the OC5 Phase II [1] and OC6  
113 Phase I projects [9]. Several proposed modifications to this original model are discussed in Section 4 to address the  
114 underpredictions. The proposed modified model is validated with a different wave condition in Section 5 followed  
115 by additional discussions and recommendations for future applications in Section 6. Finally, the conclusions are  
116 provided in Section 7.

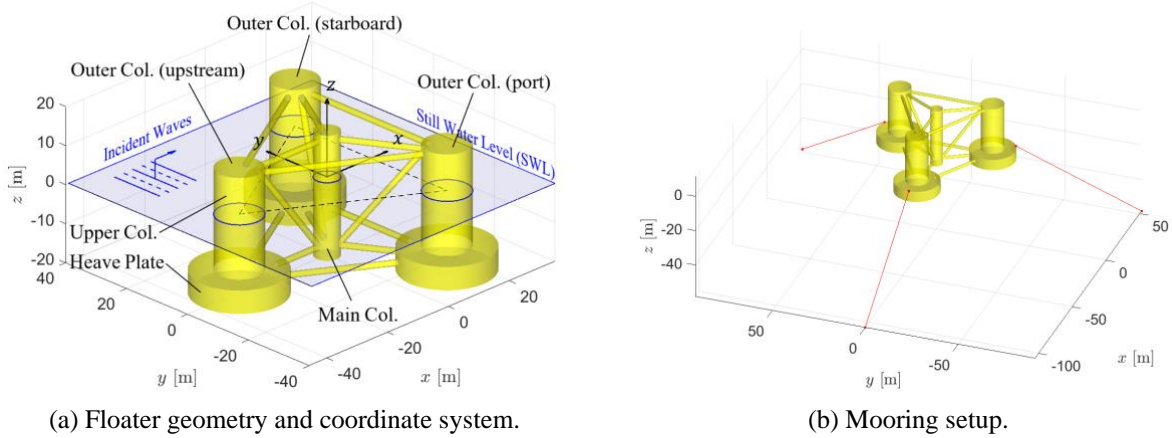
## 117 **2 Problem description**

118 The physical setup adopted for the present study closely follows the experimental campaign within OC6 Phase  
119 Ia [6,23], which included both a floating configuration with a simplified rigid tower and block mass to represent the  
120 wind turbine and a constrained condition with the substructure only (see Figure 1). The experiments were performed  
121 at 1:50 model scale; however, all dimensional values in the present article are presented at full scale based on  
122 Froude scaling. The semisubmersible design has the same geometry and draft as the OC5-DeepCwind  
123 semisubmersible [1] but slightly modified mass and inertia properties.

124 The semisubmersible in the equilibrium position, along with the adopted coordinate system, is shown in Figure  
125 2a. The platform is oriented such that a single upstream outer column faces the incident waves, and the two  
126 remaining outer columns are downstream on the port and starboard sides. The water depth is uniformly 180 m, and  
127 the gravitational acceleration is taken as  $g = 9.81 \text{ m/s}^2$ . A saltwater density of  $\rho = 1,025 \text{ kg/m}^3$  is used.

128 A global earth-fixed coordinate system,  $Oxyz$ , is adopted with the  $xy$ -plane coinciding with the calm-water  
129 surface. The origin,  $O$ , is on the centerline of the central main column in the equilibrium position, and the  $+x$ -axis

130 points along the direction of wave propagation. Because of port-starboard symmetry, the motion of the platform is  
 131 primarily in the vertical  $xz$ -plane. For the fixed condition, the wave-induced surge and heave forces are in the  $x$ - and  
 132  $z$ -directions, respectively, and the pitch moment is computed about the  $y$ -axis. For the freely floating condition, the  
 133 translation of the floater is defined by the position of the body-fixed floater reference point, which coincides with the  
 134 origin at equilibrium, in the earth-fixed coordinate system. The pitch motion is again about the  $y$ -axis.  
 135



(a) Floater geometry and coordinate system. (b) Mooring setup.  
**Figure 2.** Schematics of the physical setup. (a) Geometry of the OC6-DeepCwind semisubmersible and the adopted coordinate system for both the fixed and the freely floating configurations. (b) The taut-spring mooring setup for the floating configuration.

136 The combined dynamic properties of the semisubmersible, rigid tower, and wind turbine (represented by a  
 137 block mass in the experiment) and the mooring setup for the freely floating configuration are given in Table 1 [6].  
 138 The three taut mooring lines connected to the heave plates (shown in Figure 2b) are treated as thin and massless  
 139 linear springs. This is consistent with the actual experimental setup, which used thin, taut wires as mooring lines.  
 140 The wires went through a pulley system to connect to soft springs above water. This simplified mooring setup was  
 141 adopted by the experimental campaign specifically to minimize uncertainty and facilitate numerical modeling.

142 The floater is subjected to long-crested, irregular incident waves in the  $+x$ -direction. Two wave spectra are  
 143 considered: Joint North Sea Wave Project (JONSWAP) and white noise. The wave conditions are listed in Table 2.  
 144 In the OC6 project, the same JONSWAP wave spectrum is used for both Load Case (LC) 3.3 and LC 5.3 with the  
 145 former having a fixed floater and the latter a freely floating structure. The white-noise wave is used for LC 3.4 and  
 146 LC 5.4, again with the former denoting a fixed condition and the latter a freely floating condition. For convenience,  
 147 two frequency ranges are defined for each wave condition in Table 2: a wave-frequency range dominated by the

148 linear excitation from the incident waves and a low-frequency range primarily containing nonlinear, difference-  
 149 frequency excitation.

**Table 1.** Combined floater, tower, and turbine dynamic properties and the mooring setup of the freely floating OC6-DeepCwind semisubmersible floating offshore wind turbine. [6]

<b>Structure Dynamic Properties</b>				
Mass ( $m$ )		1.4196 $\times 10^7$ kg		
Displace Volume ( $\nabla$ )		14,053 m <sup>3</sup>		
Vertical Center of Mass ( $G_z$ )		-7.32 m		
Vertical Center of Buoyancy ( $B_z$ )		-13.15 m		
Pitch Moment of Inertia about Center of Mass ( $I_{yy}$ )		1.2979 $\times 10^{10}$ kg-m <sup>2</sup>		
Surge Natural Period		105 s		
Heave Natural Period		17.2 s		
Pitch Natural Period		31.0 s		
<b>Mooring</b>				
Unstretched line length ( $\ell_0$ )		55.432 m		
Linear spring constant ( $k$ )		4.89 $\times 10^4$ N/m		
<b>Fairleads at Equilibrium and Anchors</b>		<b>x [m]</b>	<b>y [m]</b>	<b>z [m]</b>
Fairleads	Upstream Column	-40.870	0.00	-14.00
	Starboard Column	20.434	35.39	-14.00
	Port Column	20.434	-35.39	-14.00
Anchors	Upstream Column	-105.47	0.00	-58.40
	Starboard Column	52.73	91.34	-58.40
	Port Column	52.73	-91.34	-58.40

150

**Table 2.** Incident wave conditions for both the fixed and the freely floating conditions.

<b>JONSWAP: LC 3.3 (fixed condition) and LC 5.3 (freely floating condition)</b>				
Significant Wave Height	Peak Period	Peak Enhancement Factor, $\gamma$	Low-Freq. Range	Wave-Freq. Range
7.4 m	12.0 s	3.3	0.005–0.05 Hz	0.0552–0.1345 Hz
<b>White Noise: LC 3.4 (fixed condition) and LC 5.4 (freely floating condition)</b>				
Significant Wave Height	Start Period	End Period	Low-Freq. Range	Wave-Freq. Range
6.7 m	6.0 s	26.0 s	0.005–0.036 Hz	0.0385–0.1667 Hz

151 In the current article, the OC6 project numbering of the load cases is used for brevity. To facilitate validation  
 152 against wave-basin experiments, the experimentally measured wave-elevation time series are used directly as inputs  
 153 to the OpenFAST simulations to avoid issues with statistical convergence.

### 154 **3 The underprediction of low-frequency responses by OpenFAST**

155 This article focuses on improving the ability of OpenFAST to predict the low-frequency responses of the  
 156 offshore wind semisubmersible, including both the nonlinear, low-frequency wave excitation and the surge and pitch  
 157 resonance motion of the structure. Both wave excitation and floater motion were severely underpredicted by the

158 NREL OpenFAST model developed for the OC6 Phase Ia project (referred to as the “original” model in this article)  
 159 and other mid-fidelity engineering-level tools for floating offshore wind systems [1,9]. To provide a background and  
 160 baseline for the present investigation, the original NREL OpenFAST model used by Robertson et al. [9] is described  
 161 here with the simulation results demonstrating the underprediction of the low-frequency responses. This  
 162 underprediction is addressed with several modifications to the original model as described in Section 4.

### 163 **3.1 Original OC6 OpenFAST model**

164 The original OC6 OpenFAST model developed at NREL [9] simulates the hydrodynamics of the offshore wind  
 165 semisubmersible in the time domain using a combination of second-order potential-flow theory and empirical drag  
 166 forces. The frequency-domain linear potential-flow solution, including linear wave excitation, added mass, wave  
 167 damping, and hydrostatic stiffness, was obtained using the commercial potential-flow, boundary-element solver  
 168 WAMIT V6.1 [24]. The second-order potential-flow problem was solved using WAMIT V6.107S to obtain the sum-  
 169 and difference-frequency wave-excitation QTFs. Because the second-order solution also depends on the first-order  
 170 motion response amplitude operators, two different sets of QTFs were computed for the fixed and freely floating  
 171 conditions. The use of full second-order QTFs was identified as one of the model components that consistently  
 172 improves the prediction of low-frequency structural responses and, therefore, must be included in the simulation [9].  
 173 Replacing the full QTFs with Newman’s approximation will lead to further underprediction [3,9,19]. The first-order  
 174 wave-radiation forces and moments are computed using the time convolution of the body velocities and the radiation  
 175 impulse-response function [25].

176 Two types of empirical drag force are included: distributed transverse drag force perpendicular to the column  
 177 and heave-plate centerlines, and lumped axial/normal drag forces on the two faces of the heave plates. As shown in  
 178 Figure 3, the columns and the heave plates are represented in OpenFAST by line segments along the centerline of  
 179 each member for the purpose of computing the distributed transverse drag force. Each line segment is 1 m long, and  
 180 the transverse drag force,  $\mathbf{F}_D$ , per unit length is computed at the end points of each segment using Eq. (1) [26]:

$$\mathbf{F}_D = \frac{1}{2} C_D \rho (2R) |\mathbf{v}_r - (\mathbf{v}_r \cdot \mathbf{k})\mathbf{k}| (\mathbf{v}_r - (\mathbf{v}_r \cdot \mathbf{k})\mathbf{k}), \quad (1)$$

181 where  $\mathbf{v}_r$  is the velocity vector of the incident wave field relative to the body velocity at the segment end points,  $\mathbf{k}$  is  
 182 the unit vector in the direction of the segment,  $R$  is the radius of the column or heave plate, and  $C_D$  is the drag  
 183 coefficient. A drag coefficient of  $C_D = 0.4$  is used for the upper columns and the main column, and  $C_D = 1.6$  is used

184 for the heave plates. These values were obtained by tuning the model to match the experimental surge, heave, and  
 185 pitch free-decay motions [18]. The lower value of  $C_D = 0.4$  for the upper columns is consistent with the drag  
 186 coefficient recommended by Lemmer et al. [14] for vertical cylinders, and the increased value of  $C_D = 1.6$  for the  
 187 heave plates is justified by the presence of sharp corners and strong flow separation.

188 The total transverse drag force and the resulting moment are obtained by integrating the distributed force along  
 189 the line segments. On the upper columns and the main column, the transverse drag force is integrated up to the  
 190 instantaneous first-order free surface with vertical wave stretching; that is, the wave kinematics above the still water  
 191 level is assumed to be the same as that at the still water level.<sup>3</sup> The drag force above the instantaneous free surface is  
 192 zero. The slender braces and pontoons connecting the columns and the heave plates can also be included when  
 193 calculating the distributed drag force; however, because of the small diameter, their contribution to the total wave  
 194 loads and effects on the floater motion is negligible. (Note that the slender braces and pontoons were included when  
 195 solving the first-order potential-flow solution but omitted when solving the second-order problem, as was done in  
 196 Ref. [27], because of their small diameter relative to the characteristic incident wavelength.) All results shown in the  
 197 present article were therefore obtained with the slender connecting members omitted from the drag calculation.

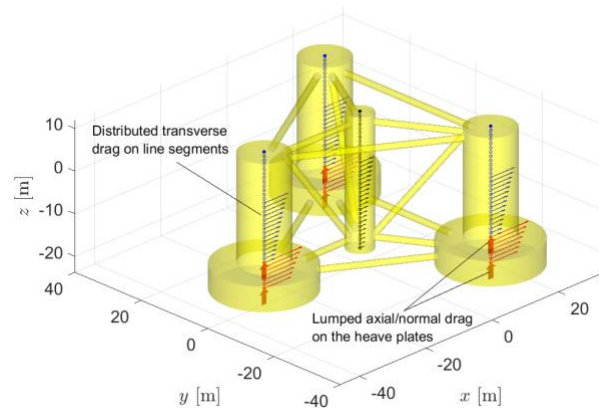


**Figure 3.** Distributed transverse drag forces and the lumped axial/normal drag forces in the OpenFAST model. The horizontal arrows represent the distributed transverse drag forces evaluated and applied along the centerlines of the columns and heave plates. The large vertical arrows represent the lumped axial/normal drag forces evaluated and applied at the end nodes of the heave plates located at the centers of the top and bottom faces of the heave plates.

<sup>3</sup> The wave-stretching capability is not available in the current publicly released version of OpenFAST; a separate development version was used in this study.

198 In addition to the distributed transverse drag, the lumped axial/normal drag forces perpendicular to the top and  
 199 bottom faces of the heave plates are applied to the end nodes of the heave plates (see Figure 3). The axial drag force,  
 200  $\mathbf{F}_{D_{Ax}}$ , is given by Eq. (2) [26] (a coefficient of 1/4 is used in place of the usual 1/2 because half of the total drag  
 201 force is applied to each side of the heave plate):

$$\mathbf{F}_{D_{Ax}} = \frac{1}{4} C_{D_{Ax}} \rho \mathbf{A} |v_{r,n}| v_{r,n}, \quad (2)$$

202 where  $\mathbf{A}$  is the normal directional face area of the heave plates pointing away from the heave plates, and

$$v_{r,n} = (\mathbf{v}_r \cdot \mathbf{A}) / |\mathbf{A}|. \quad (3)$$

203 In Eq. (3),  $\mathbf{v}_r$  is the velocity vector of the incident wave field relative to the local body velocity at the end nodes of  
 204 the heave plates, and  $v_{r,n}$  is the component of  $\mathbf{v}_r$  normal to the top or bottom faces of the heave plates. Note that  $v_{r,n}$   
 205 is positive when the normal component of the relative flow velocity points away from the heave plate. For  
 206 simplicity, the area of the bottom face of the heave plate is used for both the top face and the bottom face. The  
 207 lumped axial drag force is controlled by the axial drag coefficient,  $C_{D_{Ax}}$ , to which a value of 4.1 is assigned for both  
 208 faces despite the presence of the upper column above the heave plate. This is because Zhang and Ishihara [28]  
 209 showed that, for a similar column/heave plate geometry, the heave-plate drag coefficient remains approximately  
 210 constant when the ratio of the heave-plate diameter to the upper-column diameter is greater than 2 (this ratio is  
 211 exactly 2 for the present geometry), suggesting limited influence from the presence of the upper column; therefore, it  
 212 is physically justifiable to use the same reference area and drag coefficient for both the top and bottom faces of the  
 213 heave plates for the present geometry. The drag coefficient of 4.1 was again tuned based on free-decay experiments  
 214 [18]. (In [9,18], the doubled axial drag coefficient of 8.2 was reported. This is because the drag force was only  
 215 applied to the bottom face of the heave plates, which led to results effectively identical to Figure 4 obtained with the  
 216 drag force applied to both the top and bottom faces but with half the drag coefficient, 4.1.) The relatively low  $C_{D_{Ax}}$   
 217 is a consequence of the large thickness of the heave plates; the drag coefficient of heave plates tends to decrease  
 218 with an increasing thickness-to-diameter ratio [28]. Note that different combinations of the face area and drag  
 219 coefficients can be used to obtain effectively identical results. For example, if the actual smaller area of the top face  
 220 of the heave plate is used, a larger drag coefficient can be assigned to the top face compared to that for the bottom

221 face to obtain the same result. The axial drag on the bottom of the main column has little effect on the floater  
222 response because of the much smaller area relative to the heave plates; therefore, this force is neglected.

223 For the freely floating condition, the OpenFAST simulations have full six-degrees-of-freedom structural  
224 motion, but only surge, heave, and pitch motions are excited because of port-starboard symmetry. In addition to the  
225 wave-radiation damping and the distributed/lumped drag, global linear damping coefficients of 75 kN·s/m in surge  
226 and 31 MN·m·s/rad in pitch are included in the model following [9,18]. The added damping provides the correct  
227 linear damping characteristics of the model during small-amplitude free-decay oscillation. For the sake of  
228 consistency with past investigations and to retain the model characteristics in calm water, the added damping is  
229 retained in the present investigation.

### 230 **3.2 The underprediction of low-frequency responses by the original OC6 model**

231 To demonstrate the underprediction identified in [1,9], we first consider the JONSWAP irregular waves  
232 described in Table 2. The wave loads on the offshore wind platform when constrained (LC 3.3) and the motion of  
233 the platform when freely floating (LC 5.3) are computed using the original OpenFAST model described in Section  
234 3.1. The resulting power spectral densities (PSDs) are shown in Figure 4. Whereas the model generally predicts the  
235 wave-frequency (blue regions in Figure 4) responses of the structure well, the OpenFAST model severely  
236 underpredicts the surge force when compared to the experiment by almost one order of magnitude in the low-  
237 frequency region (the pink region in Figure 4a). While not as severe, the low-frequency pitch moment (Figure 4b) is  
238 also consistently underpredicted by the model by approximately 17% (which corresponds to a 30% underprediction  
239 of the pitch moment PSD). The underpredicted low-frequency wave load from OpenFAST is at least partially  
240 responsible for the underprediction of the low-frequency surge and pitch resonance motions (Figure 4c and 4d); the  
241 overprediction of the damping or drag in surge and pitch might also play a role.

242 The underprediction of the low-frequency loads and responses is not unique to OpenFAST. It was observed, to  
243 varying degrees, for a host of state-of-the-art, mid-fidelity engineering-level tools from more than two dozen  
244 academic and research institutions and industry partners [9,29]. The error in the model predictions resulted in a 10%  
245 to 20% underprediction of the global ultimate and fatigue loads [1]; therefore, the engineering models cannot  
246 reliably be used for design optimization purposes. The current article focuses on addressing this limitation of the  
247 engineering models to obtain better predictions in the low-frequency region.

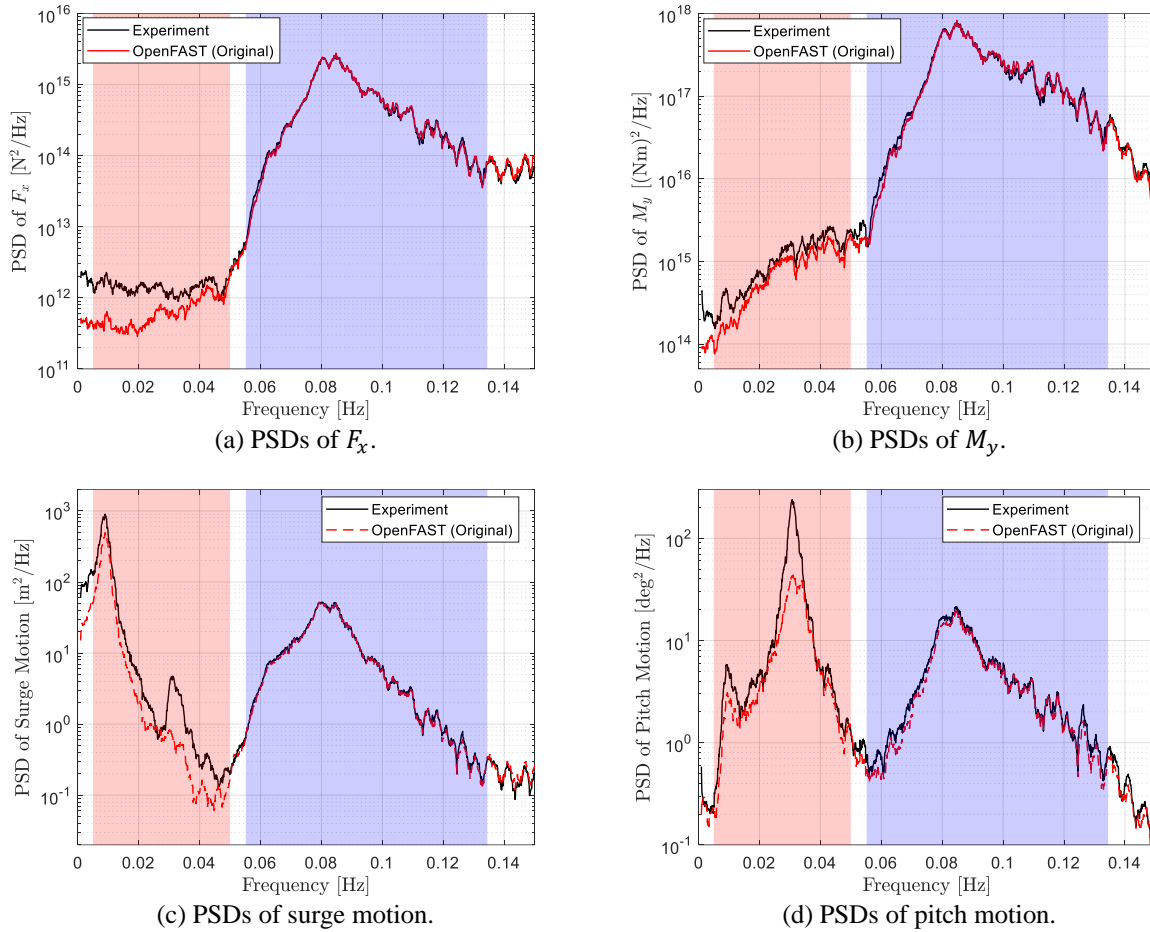


**Figure 4.** Power spectral densities (PSDs) of the wave-induced (a) surge force,  $F_x$ , and (b) pitch moment,  $M_y$ , on the DeepCwind offshore wind platform when constrained (LC 3.3), and PSDs of (c) surge motion and (d) pitch motion of the platform when freely floating (LC 5.3). The pink region indicates the low-frequency range, and the blue region is the wave-frequency range (see Table 2). The original OpenFAST model of [9] is described in Section 3.1.

#### 248 **4 Modifications to the original OpenFAST model to improve low-frequency predictions**

249 In this section, we propose several modifications to the modeling practice and model formulation of OpenFAST  
 250 to address the deficiencies of the original OC6 model described in Section 3. There are, of course, multiple ways to  
 251 achieve better agreement with the experiment. For instance, as proposed in Ref. [9], we can artificially modify and  
 252 scale up the QTFs from the second-order potential-flow theory to increase the difference-frequency wave excitation  
 253 without changing the wave-frequency responses. This has been applied to a fixed structure to good effect by Li and  
 254 Bachynski-Polić [21]; however, this approach also leads to substantial challenges with model tuning. It is difficult to  
 255 know how we should modify the QTFs without extensive a priori knowledge of the system behavior from either

256 wave-basin experiments or CFD simulations; therefore, in this article we attempt to devise modifications to the  
257 original model that are physically justifiable and, ideally, that also have minimal complexity to avoid further  
258 complicating model tuning as much as possible. Finally, we would like to have a reasonably general model that  
259 applies to a range of similar wave conditions and floater configurations, including both fixed and freely floating,  
260 without extensive retuning of the model.

261 A PSD-integral metric,  $S_{int}$ , is used to quantitatively gauge the agreement between the OpenFAST predictions  
262 and the experimental measurements [9]:

$$S_{int} = \int_{f_0}^{f_1} S(f) df, \quad (4)$$

263 where  $S(f)$  is the one-sided, unsmoothed, PSD of any quantity of interest (force, moment, motion, and so on). The  
264 integration over frequency,  $f$ , is performed over either the low-frequency range or the wave-frequency range  
265 specified in Table 2 for each wave condition. For consistency, all PSDs and PSD integrals shown in this article were  
266 computed from the same 3-hour time window after an initial transient phase was removed. The PSD integral can be  
267 thought of as the standard deviation of the quantity of interest over a given frequency range.

268 The uncertainties in  $S_{int}$  were also recomputed for the experimental results following the procedure described in  
269 Ref. [6] to facilitate comparison with model predictions. In Ref. [6], eight physical parameters in the experiment  
270 with significant levels of systematic uncertainty were identified that potentially had nonnegligible effects on the  
271 response metric  $S_{int}$ : wave excitation, longitudinal and vertical positions of the center of mass of the physical model,  
272 pitch moment of inertia, column/heave plate diameter, model draft, model mass, and the mooring spring constant.  
273 The estimated experimental uncertainties of these parameters were propagated to  $S_{int}$  using numerical models and  
274 combined in quadrature, assuming independent sources of error to obtain the total experimental uncertainties;  
275 however, in contrast to Ref. [6], which used four different mid-fidelity engineering models to propagate the  
276 uncertainty, only the final improved OpenFAST model described in this article was used to propagate the  
277 uncertainties here. Furthermore, the random uncertainty in the experimental results, which was found to be  
278 negligible compared to the systematic part [6], is neglected.

279

#### 280 **4.1 Wave stretching and depth-dependent transverse drag coefficient**

281 We first focus on the underprediction of the low-frequency surge force on the fixed structure (LC 3.3). As part  
282 of OC6 Phase I, a coordinated investigation with both high-fidelity CFD simulations and wave-basin experiments

283 was carried out to better understand the nonlinear, difference-frequency wave excitation on a constrained offshore  
284 wind semisubmersible in bichromatic waves [10–12] using a similar floater geometry. During this study, we  
285 identified that near the surge resonance frequency (0.01 Hz) of the structure, the nonlinear surge force primarily  
286 comes from the viscous drag on the structure, whereas second-order wave diffraction has negligible contribution.  
287 Based on this observation, we focus on the transverse drag force to address the underprediction of the low-frequency  
288 surge force on the constrained platform.

289 We performed a sensitivity study to better understand the relation between the transverse drag coefficient and  
290 the low-frequency surge force. The transverse drag coefficient on the upper columns and the main column is altered,  
291 whereas that on the heave plate is kept constant at 1.6, as in Section 3.1, throughout the present investigation.  
292 Because of the exponentially decaying wave-field velocity with depth, the transverse drag on the heave plates has  
293 little contribution to the low-frequency surge force when the structure is fixed. The sensitivity study was done both  
294 with and without vertical wave stretching for the computation of the transverse drag force. The PSDs of surge force  
295 from this sensitivity study are shown in Figure 5, and the corresponding PSD integrals are compared in Figure 6.

296 As shown in Figure 5a, the low-frequency surge force is relatively insensitive to the transverse drag coefficient  
297 on the upper columns and the main column without wave stretching. A very high drag coefficient of  $C_D = 4$  is  
298 needed to obtain a low-frequency surge-force PSD integral comparable to that of the experiment (Figure 6a).  
299 Further, the surge-force PSD from the OpenFAST simulation does not match the experimental measurements in the  
300 low-frequency range (Figure 5a). Finally, the high  $C_D$  leads to an overprediction of the wave-frequency surge force  
301 (Figure 6a) because of excessive viscous loads. All observations suggest that simply increasing the value of  $C_D$  is  
302 not the correct approach.

303 On the other hand, when vertical wave stretching is enabled, the low-frequency surge force becomes more  
304 sensitive to  $C_D$ . With  $C_D = 1.6$ , good agreement is observed between the experiment and the OpenFAST prediction  
305 both in terms of the low-frequency surge-force PSD (Figure 5b) and PSD integral (Figure 6b), lending confidence to  
306 the correctness of the model. The wave-frequency surge excitation from the model remains in good agreement with  
307 the experiment as well. Furthermore, it can be concluded that the low-frequency surge force predominantly comes  
308 from the transverse drag force on the columns near the waterline in the periodically wetted zone, a third-order  
309 contribution, rather than from the submerged sections of the columns.

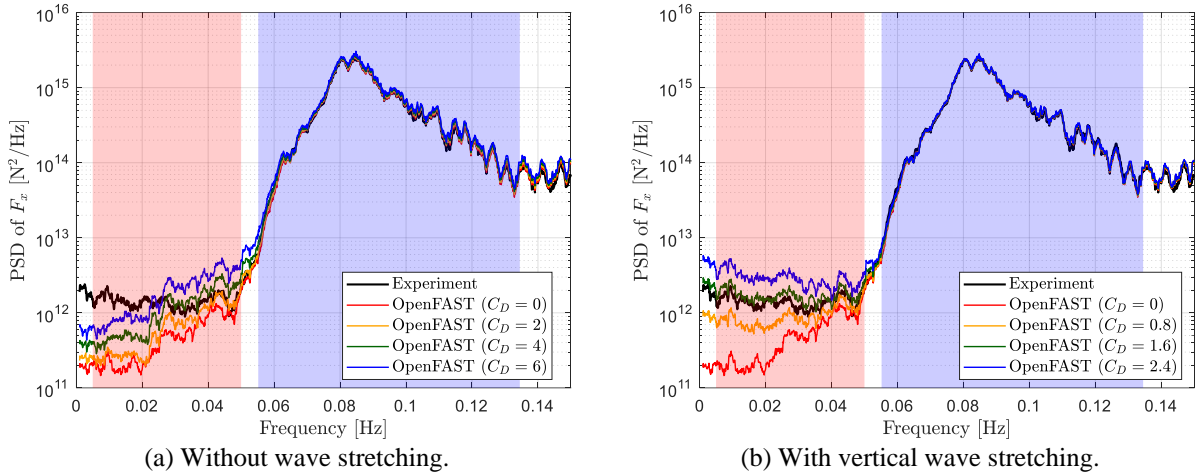


**Figure 5.** Sensitivity of the surge force,  $F_x$ , on the fixed semisubmersible to the transverse drag coefficient,  $C_D$ , on the upper columns and the main column (a) without vertical wave stretching and (b) with vertical wave stretching. The structure is in the irregular waves of LC 3.3. The pink region indicates the low-frequency range, and the blue region is the wave-frequency range (see Table 2).

310

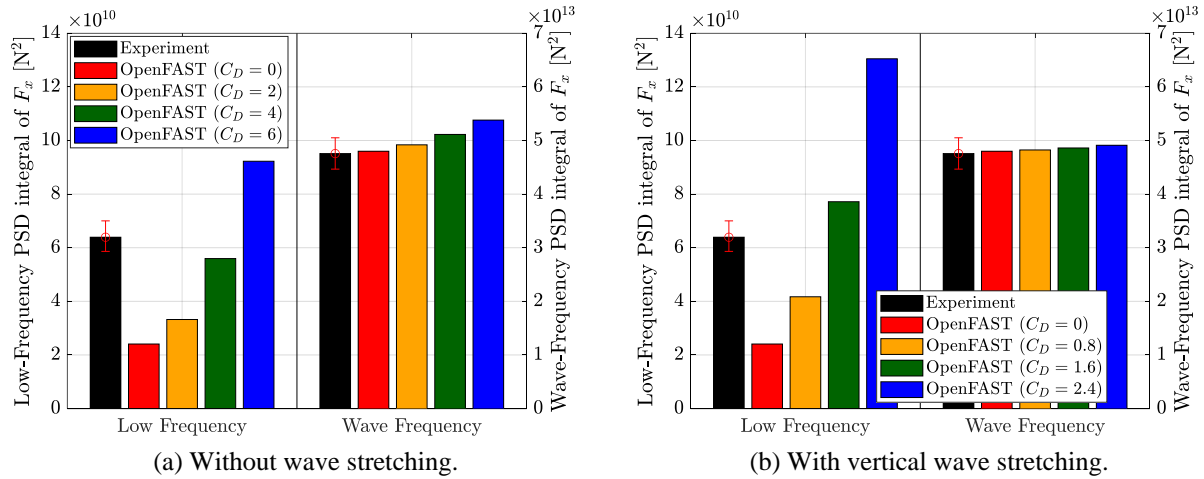


**Figure 6.** Sensitivity of the PSD-integral metrics of the surge force,  $F_x$ , on the fixed semisubmersible to the transverse drag coefficient,  $C_D$ , on the upper columns and the main column (a) without vertical wave stretching and (b) with vertical wave stretching. The structure is in the irregular waves of LC 3.3.

311 Whereas increasing  $C_D$  to 1.6 on the upper columns provides a good prediction of the low-frequency surge force  
 312 with vertical wave stretching, it will result in incorrect surge free-decay behavior, which requires a drag coefficient  
 313 of 0.4 [18]. We therefore propose the use of a depth-dependent transverse drag coefficient. For the permanently  
 314 submerged portion of the columns (approximately defined as  $z < -4$  m), the original value of  $C_D = 0.4$  is used. The

315 value of  $C_D$  is increased to 1.6 in the periodically wetted zone ( $z > -3$  m) as shown in Figure 7. With this approach,  
 316 the OpenFAST model retains the correct behavior in surge free-decay and forced motion (see the NREL solutions in  
 317 Ref. [9]) while predicting the correct low-frequency surge force when compared to the experiment.  
 318

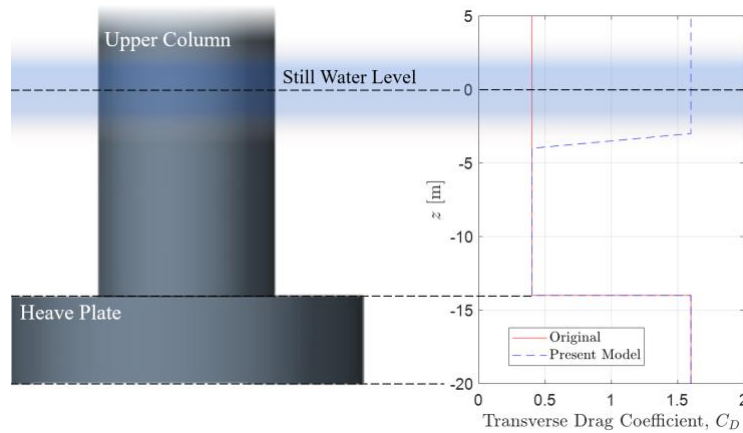


**Figure 7.** Distribution of the transverse drag coefficient,  $C_D$ , along the upper column and heave plate. Compared to the original OC6 model [9,18], the present model uses depth-dependent  $C_D$  on the upper columns with increased drag coefficient in the periodically wetted zone (the blue shaded region).

319 The increased drag coefficient near the still water level is physically justifiable because the proximity to the free  
 320 surface could lead to an increase in the effective sectional drag coefficient. This behavior has been observed with a  
 321 vertical surface-piercing circular cylinder in a steady current [30] and, more recently, in regular waves [31]. This  
 322 possible increase in the effective sectional drag coefficient warrants further detailed investigation that is beyond the  
 323 scope of the present article.

324 With the depth-dependent transverse drag coefficient, the predicted wave force in surge is shown in Figure 8  
 325 with comparison to the original OC6 OpenFAST model described in Section 3.1. A significantly improved  
 326 prediction of the low-frequency surge force is achieved with the present model without affecting the wave-frequency  
 327 surge force. Furthermore, the model also automatically generates greatly improved predictions of the floater surge  
 328 motion under the freely floating condition (LC 5.3), lending more confidence to this modeling approach. The PSD  
 329 and PSD integral of the surge motion are shown in Figure 9. The agreement between the experiment and the present  
 330 OpenFAST prediction is very encouraging. This comparison indicates that the underprediction of surge resonance  
 331 motion previously observed [1,9] is primarily a consequence of underpredicting the low-frequency surge excitation  
 332 rather than of overpredicting the surge damping. Note that if the additional global linear damping in surge of 75  
 333 kN·s/m discussed in Section 3.1 is removed, the prediction of the low-frequency surge PSD integral by the present

334 modified OpenFAST model will increase by approximately 21%, which corresponds to a 10% increase in the surge  
 335 resonance amplitude. The added damping has a negligible effect on the wave-frequency surge response.

336

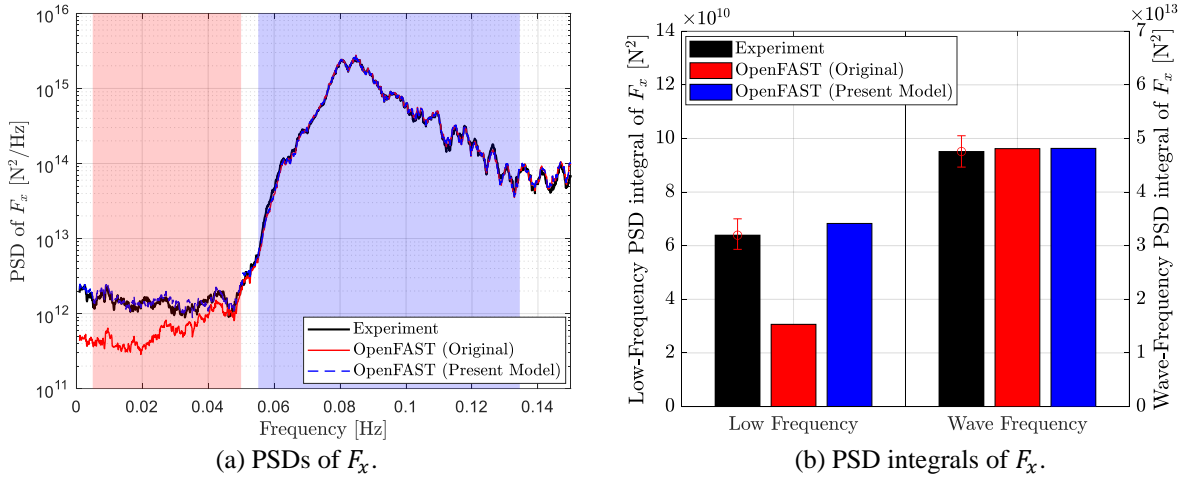


**Figure 8.** Surge force,  $F_x$ , on the fixed semisubmersible in irregular waves (LC 3.3). (a) The PSDs of  $F_x$  are shown, with the pink region indicating the low-frequency range and the blue region indicating the wave-frequency range (see Table 2). (b) The PSD integrals of  $F_x$  are compared. The original OpenFAST model of [9] is described in Section 3.1. The present model utilizes the depth-dependent transverse drag coefficient.

337 Taking a step further, the time histories of the surge motion from the experiment and model predictions are  
 338 compared in Figure 10. The phase of the low-frequency surge resonance motion is also consistent between the  
 339 experiment and the present model. In comparison, the original model visibly underpredicts the low-frequency surge  
 340 resonance.

341 The use of a depth-dependent transverse drag coefficient has a negligible effect on the model predictions in  
 342 heave and pitch, which means the increased drag coefficient near the waterline can be tuned independently to  
 343 provide the correct level of low-frequency surge force and motion without any unexpected side effects. This greatly  
 344 simplifies model tuning, which needs to be performed for different column cross-section geometries and, to a lesser  
 345 extent, different wave conditions as demonstrated in Section 5.

346 The use of a depth-dependent transverse drag coefficient is not a new idea. This feature is readily available in  
 347 the current version of OpenFAST and has been successfully applied to model the slow drift motion of floating  
 348 offshore wind semisubmersibles in several prior investigations with a different floater geometry [15–17]; however,  
 349 these prior studies directly tuned the drag coefficient against the experimental slow-drift motion without explicitly  
 350 considering the low-frequency surge force on a fixed structure. In the present study, we have shown that the use of a

351 depth-dependent drag coefficient can also lead to good agreement in the surge wave force on a fixed structure over  
 352 the entire low-frequency region, and the same distribution of transverse drag coefficient automatically results in the  
 353 correct low-frequency surge motion. This observation bolsters our confidence in the use of a depth-based drag  
 354 coefficient.

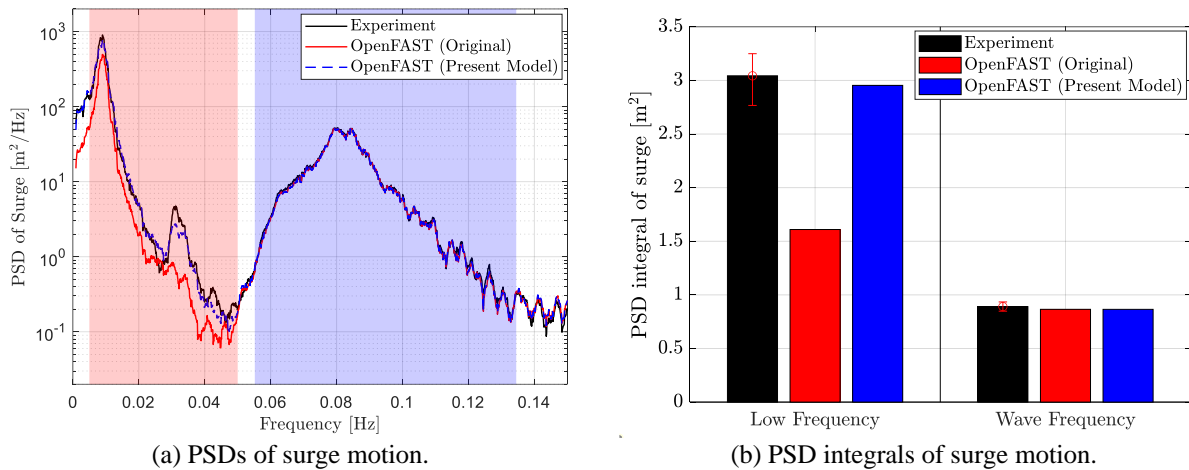


**Figure 9.** Surge motion of the freely floating offshore wind semisubmersible in irregular waves (LC 5.3). (a) The PSDs of the surge motion are shown, with the pink region indicating the low-frequency range and the blue region indicating the wave-frequency range (see Table 2). In (b), the PSD integrals of the surge motion are compared. The original OpenFAST model of [9] is described in Section 3.1. The present model utilizes the depth-dependent transverse drag coefficient.

355

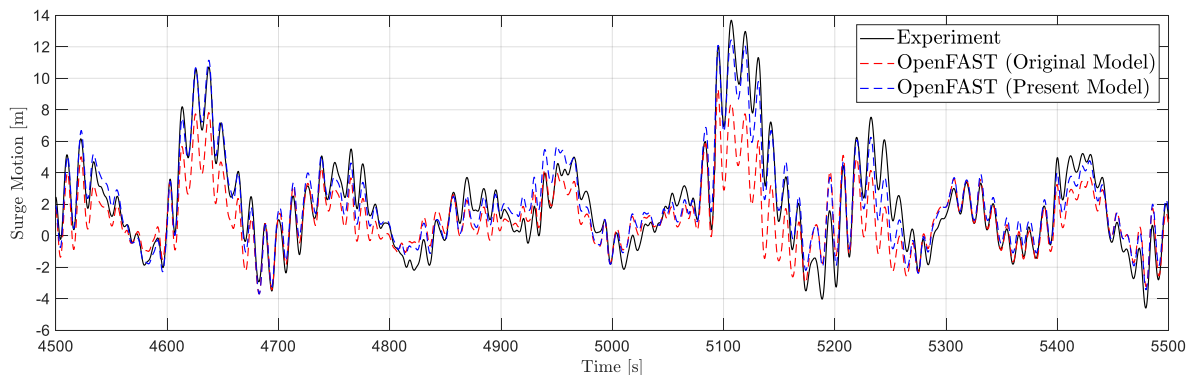


**Figure 10.** Time series of the surge motion of the offshore wind semisubmersible in irregular waves (LC 5.3). The present model utilizes the depth-dependent transverse drag coefficient.

356

## 357 4.2 Modification to the axial drag force on the heave plates

358 As shown in Figure 4b, the underprediction of the low-frequency pitch moment on the fixed structure is not as  
 359 severe when compared to the surge force. Most of the low-frequency pitch moment has already been captured by the

360 second-order potential-flow QTF. The remaining difference between the experiment and the OpenFAST predictions  
361 is most likely a consequence of unsatisfactory modeling of the axial/normal drag force on the heave plates, which is  
362 addressed in this section.

363 The sensitivity of the low-frequency pitch moment to the heave-plate axial drag coefficient  $C_{D_{Ax}}$  is investigated  
364 in Figure 11. The low-frequency pitch moment is not very sensitive to the axial drag coefficient as shown in Figure  
365 11a above 0.02 Hz, and the underprediction persists even with a very high drag coefficient of 8, as indicated by the  
366 low-frequency pitch-moment PSD integral in Figure 11b. With  $C_{D_{Ax}} = 8$ , the wave-frequency pitch moment is  
367 already significantly overpredicted. The heave force (not shown) also shows a very large error. This observation is  
368 consistent with that from Ref. [21], which states that the axial drag forces on the heave plates primarily affect the  
369 pitch moment at the wave frequencies with only minor effects on the difference/low-frequency pitch moment. In  
370 fact, only the pitch moment near the very low surge natural frequency, 0.01 Hz, is weakly influenced by  $C_{D_{Ax}}$ ,  
371 whereas the moment at the more relevant pitch natural frequency around 0.032 Hz is hardly affected at all. This  
372 behavior is also noted in Ref. [29]. This sensitivity study demonstrates that it is impossible to obtain satisfactory  
373 predictions of the pitch moment over both low frequencies and wave frequencies simultaneously by simply tuning  
374 the heave drag coefficient,  $C_{D_{Ax}}$ . Modifications to the existing formulation of the axial drag force were therefore  
375 investigated.

376 The existing axial-drag formulation used by OpenFAST is given in Section 3.1. One important feature is that  
377 the axial drag forces are evaluated and applied to both faces of the heave plates (top and bottom) as shown in Figure  
378 3, with half of the drag force on each face. This formulation is originally designed for Morison-equation-only  
379 members, meaning members not included in the potential-flow solution whose effects are only accounted for  
380 through the Morison equation. For such parts, this is an appropriate model. When the flow normal to the surface is  
381 directed toward the surface ( $v_{r,n} < 0$ ), the force represents the effect of increased stagnation pressure on the surface.  
382 When the flow is directed away from the surface ( $v_{r,n} > 0$ ), the force represents the low pressure on the surface  
383 caused by flow separation and a lack of pressure recovery; however, this formulation is not entirely appropriate for  
384 hybrid members, which are members already included in the potential-flow calculation with added empirical viscous  
385 drag forces. For such components, the contribution from the increased stagnation pressure on the face with  $v_{r,n} < 0$   
386 is already accounted for in the hydrodynamic coefficients from the potential-flow solution, which also has perfect  
387 pressure recovery on the opposite face with  $v_{r,n} > 0$  because of a lack of viscous effects and flow separation;

388 therefore, the additional axial viscous drag force for such parts should only approximate the difference between the  
 389 potential-flow solution and the real viscous flow on the face with  $v_{r,n} > 0$ , caused by flow separation.

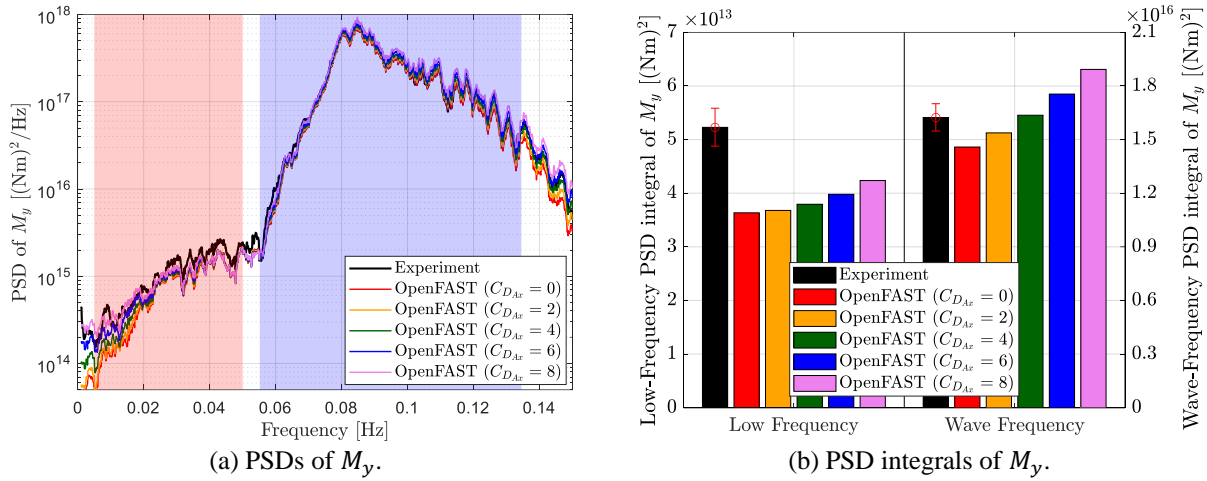


**Figure 11.** Sensitivity of the (a) PSD and (b) PSD integrals of the pitch wave moment on the fixed offshore wind semisubmersible to the axial drag coefficient of the heave plates,  $C_{D_{Ax}}$ . The floater is in irregular wave (LC 3.3). In (a), the pink region indicates the low-frequency range, and the blue region is the wave-frequency range (see Table 2).

390 In other words, it is more appropriate to evaluate and apply the total axial drag force only on the face of the  
 391 heave plates with  $v_{r,n} > 0$  (i.e., the flow is directed away from the surface). Based on this argument, Eq. (2) is  
 392 slightly modified:

$$\mathbf{F}_{D_{Ax}} = \frac{1}{2} C_{D_{Ax}} \rho \mathbf{A} |v_{r,n}| \max(v_{r,n}, 0). \quad (5)$$

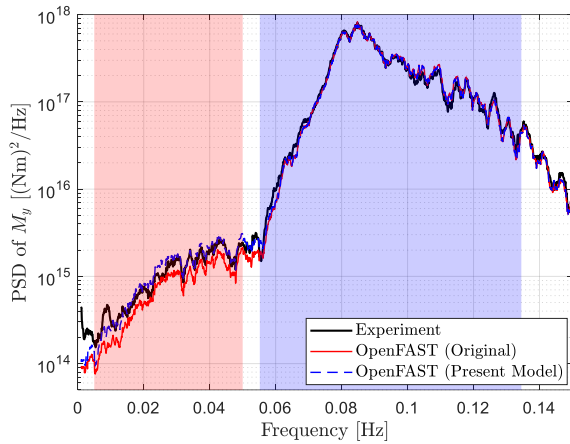
393 Numerically, doubling the lead coefficient of  $\frac{1}{4}$  in Eq. (2) to  $\frac{1}{2}$  in Eq. (5) ensures that the modified formulation of  
 394 Eq. (5) will provide the same drag force as the original Eq. (2) for a hypothetical uniform and constant flow normal  
 395 to the heave plates with the same  $C_{D_{Ax}}$ , because we are only applying the force on the face with  $v_{r,n} > 0$  instead of  
 396 on both faces, top and bottom. Physically, doubling the drag force is also consistent with the fact that the perfect  
 397 pressure recovery in the potential-flow solution on the face with  $v_{r,n} > 0$  increases the discrepancy with the real  
 398 viscous flow, which has a pressure drop from flow separation instead of an increase.

399 One interesting observation is that the effect of the proposed modification to the axial drag force diminishes  
 400 with a decrease in the thickness of the heave plates. As the thickness of the heave plate approaches zero, the  
 401 modified axial drag force will reduce to the original formulation of Eq. (2); however, for the thick heave plates of

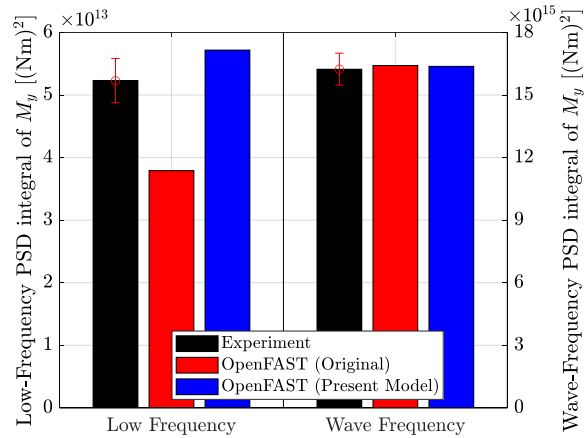
402 the DeepCwind floater considered in the present study, the variation of the background incident wave-field velocity  
403 with depth is not negligible across the height of the heave plate, and the modified formulation of Eq. (5) results in  
404 small changes in the time history of the modeled heave-plate drag force.

405 In the present study, the large heave plates are included in the potential-flow computation; therefore, the axial  
406 drag force is calculated using Eq. (5) in the present modified model with the original axial drag coefficient of  
407  $C_{D_{Ax}} = 4.1$  from Section 3.1. The pitch excitation on the fixed structure (LC 3.3) as predicted by the present  
408 OpenFAST model is compared to the experimental measurements in Figure 12. Interestingly, the proposed change  
409 to the axial drag closed the gap between the experimental and the model-predicted moment in the low-frequency  
410 region. The modification also has little effect on the wave-frequency moment, which is the desired behavior. To  
411 further illustrate the effect of Eq. (5) on the pitch moment,  $M_y$ , the PSDs of the contribution to  $M_y$  from the axial  
412 drag forces on the heave plates only are shown in Figure 13. Comparing the results from Eq. (2) and Eq. (5), the  
413 largest relative increase in pitch moment obtained with Eq. (5) is between 0.01 Hz and 0.055 Hz, which exactly  
414 corresponds to the low-frequency range over which the nonlinear pitch moment is underpredicted by the original  
415 OpenFAST model, whereas the pitch moment in the wave-frequency range is hardly affected. To be exact, the use of  
416 Eq. (5) also slightly increases the pitch moment near the wave peak frequency of 0.083 Hz; however, the increase in  
417 pitch moment at the peak frequency is actually less than that in the low-frequency range near 0.047 Hz, which,  
418 coupled with the much higher level of pitch moment at the wave frequencies, results in negligible relative changes in  
419 the pitch moment. The fact that Eq. (5) leads to an increase in the nonlinear pitch moment over the correct frequency  
420 range lends further confidence to the proposed change to the axial drag force.

421 With the modified axial-drag formulation, the OpenFAST model is used to simulate the floater under a freely  
422 floating condition in irregular waves (LC 5.3). Compared to the original model, the predicted pitch resonance  
423 motion, shown in Figure 14, is higher and agrees better with the experimental measurements because of the  
424 increased low-frequency pitch moment; however, the pitch motion is still underpredicted, suggesting that pitch  
425 damping is also overestimated at the pitch resonance frequency. This last issue is addressed in Section 4.3.



(a) PSDs of  $M_y$ .



(b) PSD integrals of  $M_y$ .

**Figure 12.** Pitch moment,  $M_y$ , on the fixed offshore wind semisubmersible in irregular waves (LC 3.3). (a) The PSDs of  $M_y$  are shown, with the pink region indicating the low-frequency range and the blue region indicating the wave-frequency range (see Table 2). In (b), the PSD integrals of  $M_y$  are compared. The original OpenFAST model of [9] is described in Section 3.1. The present model is based on the modified axial drag of Eq. (5).

426

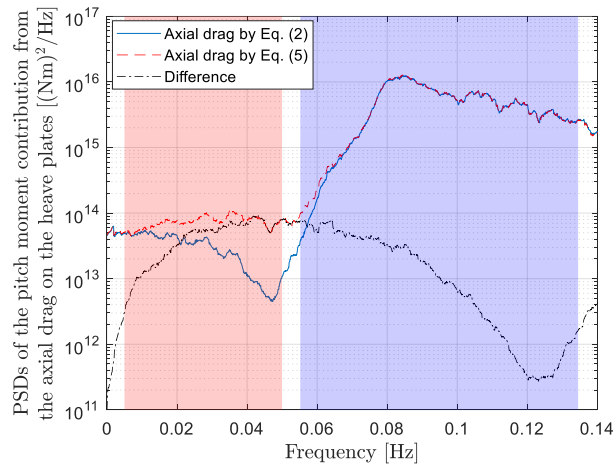


**Figure 13.** Comparison of the PSDs of the pitch moment contributed by the axial drag force on the heave plates. The axial drag force is evaluated by the original OpenFAST formulation of Eq. (2) and the modified formulation of Eq. (5). The PSD of the difference between the results obtained using the two equations is also shown.

427

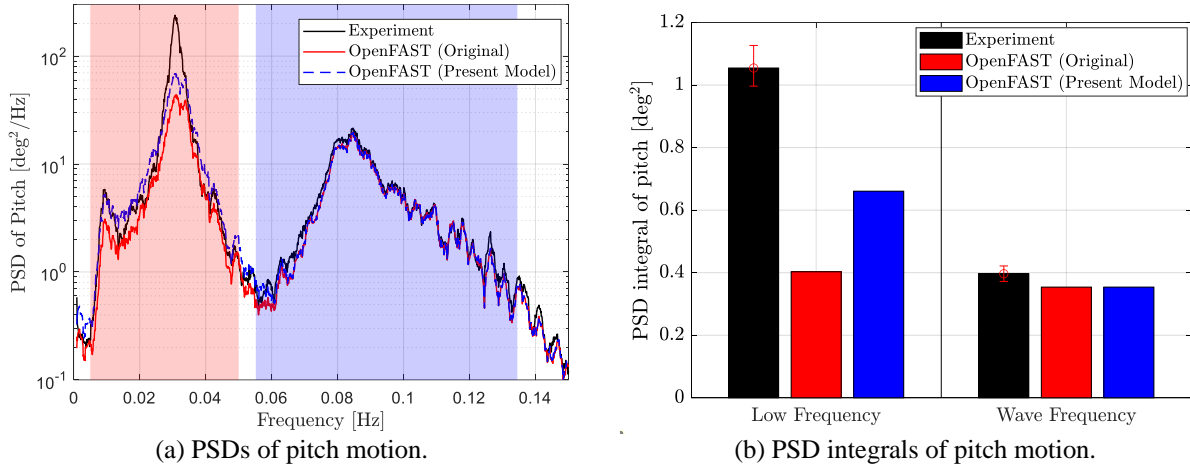


**Figure 14.** Pitch motion of the freely floating offshore wind semisubmersible in irregular waves (LC 5.3). (a) The PSDs of the pitch motion are shown, with the pink region indicating the low-frequency range and the blue region indicating the wave-frequency range (see Table 2). In (b), the PSD integrals of the pitch motion are compared. The original OpenFAST model of [9] is described in Section 3.1. The present model is based on the modified axial drag of Eq. (5).

428

### 4.3 High-pass velocity filter for the drag force on the heave plates

429 To better understand the effects of the heave-plate axial drag coefficient, the freely floating structure in irregular  
 430 waves (LC 5.3) was simulated with three different values of  $C_{D_{Ax}}$  by the present OpenFAST model with the  
 431 modified axial-drag formulation described in Section 4.2. The resulting heave and pitch motions of the floater are  
 432 shown in Figure 15. It is apparent that a low drag coefficient of  $C_{D_{Ax}} = 1.6$  leads to better predictions of the pitch  
 433 resonance motion at 0.032 Hz; however, the low drag coefficient leads to an overprediction of the heave resonance  
 434 motion near 0.058 Hz. This is essentially the same issue encountered in Ref. [18], which suggested that the heave  
 435 and pitch resonance motions require conflicting axial drag coefficients for the heave plates; however, this apparent  
 436 conflict is likely not between the two modes of motion, rather it is the different frequency bands that require  
 437 different drag coefficients. This is apparent from the results with the highest axial drag coefficient of  $C_{D_{Ax}} = 7.2$ ,  
 438 which show improved predictions of both the heave and pitch motions at the higher wave peak frequency of 0.083  
 439 Hz.  
 440

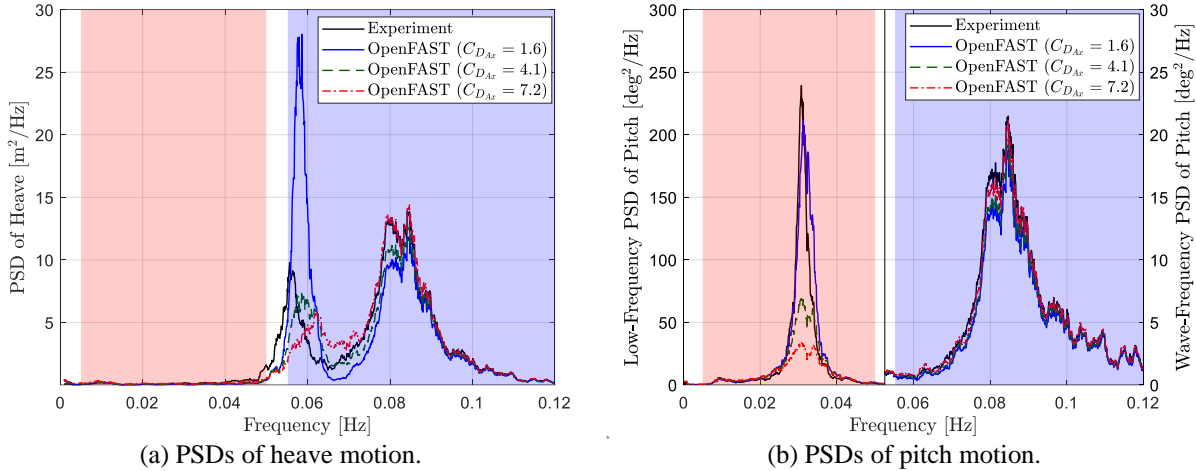


**Figure 15.** PSDs of (a) heave motion and (b) pitch motion of the freely floating offshore wind semisubmersible in irregular waves (LC 5.3) with different axial drag coefficients,  $C_{D_{Ax}}$ . The axial drag was computed using Eq. (5). Note that in (b), two different scales are used for the low- and wave-frequency ranges.

441 This observation shows that different axial-drag coefficients work better for different frequency ranges, with  
 442 lower frequency motion requiring a lower drag coefficient. This frequency dependence of the drag coefficient might  
 443 be explained by the fact that the flow separation and alternate vortex shedding at the sharp corners of the heave  
 444 plates are mostly controlled by the more rapid wave-frequency flow and body oscillation rather than by the slow  
 445 body oscillation at the much lower pitch resonance frequency. It is therefore conceivable that the drag force would  
 446 be more closely linked to the wave-frequency velocity components and react less strongly to the low-frequency  
 447 velocity components, resulting in a higher effective drag coefficient for the former and a lower coefficient for the  
 448 latter. This effect associated with the simultaneous presence of velocity components at multiple frequencies is likely  
 449 distinct from the usual dependence of drag coefficient on the Keulegan-Carpenter (KC) number in harmonic flows.  
 450 Furthermore, in a realistic, irregular-wave environment where the definition of the KC number is not  
 451 straightforward, the KC-number effect is usually associated with the overall level of wave and structural motion  
 452 amplitudes in the literature and tied to different sea states (see, e.g., Ref. [32]) rather than different frequency bands  
 453 of a given sea state.

454 Whereas a frequency-dependent drag coefficient can be implemented in the frequency domain with linearized  
 455 drag and an iterative solution, it is challenging to implement a proper frequency-dependent drag coefficient in a  
 456 time-domain model like OpenFAST with quadratic drag forces. Boon [33] developed an alternative form of the  
 457 Morison equation to include frequency-dependent drag coefficients for a fixed, surface-piercing vertical cylinder;

458 however, it is difficult to apply to a floating structure when the relative flow velocity is not known a priori. Instead,  
 459 we propose a simplified approach that approximates the required behavior of the heave-plate drag force to capture  
 460 the low-frequency pitch resonance motion without adversely affecting the prediction of the heave resonance motion.  
 461 This is achieved with the help of a simple first-order high-pass filter for the relative normal velocity  $v_{r,n}$  in Eq. (5).  
 462 Higher-order passive filters are not recommended because of the excessive phase shift. The filter equation in  
 463 discrete time is given by

$$\tilde{v}_{r,n}^i = C\tilde{v}_{r,n}^{i-1} + C(v_{r,n}^i - v_{r,n}^{i-1}), \quad (6)$$

464 where  $i$  is the time-step number and  $\tilde{v}_{r,n}^i$  is the filtered relative normal velocity. The filter coefficient,  $C$ , is given by

$$C = \exp(-2\pi f_c/f_s), \quad (7)$$

465 where  $f_c$  and  $f_s$  are the cutoff frequency and sampling frequency (inverse of time step), respectively.

466 Note that it is important to filter the relative velocity rather than the drag force itself. The latter approach will  
 467 also remove the low-frequency viscous moment in pitch on a fixed structure. The former will leave the low-  
 468 frequency pitch moment shown in Section 4.2 mostly unaffected because the low-frequency viscous excitation  
 469 primarily comes from the quadratic interaction of the wave-frequency velocity components that are weakly affected  
 470 by the high-pass filter. Only the drag force induced by the low-frequency velocity component is reduced, following  
 471 the rationale that the flow separation and vortex shedding at the corners of the heave plates and, by extension, the  
 472 heave-plate drag force responds more strongly to the wave-frequency flow velocity and body oscillation. With the  
 473 filtered relative velocity,  $\tilde{v}_{r,n}$ , the axial drag force is given by

$$\mathbf{F}_{D_{Ax}} = \alpha\mathbf{F}_{D_{Ax,0}} + (1 - \alpha)\mathbf{F}_{D_{Ax,f}}, \quad (8)$$

474 where

$$\mathbf{F}_{D_{Ax,0}} = \frac{1}{2}C_{D_{Ax}}\rho\mathbf{A}|v_{r,n}|\max(v_{r,n}, 0) \quad (9)$$

475 and

$$\mathbf{F}_{D_{Ax,f}} = \frac{1}{2}C_{D_{Ax}}\rho\mathbf{A}|\tilde{v}_{r,n}|\max(\tilde{v}_{r,n}, 0). \quad (10)$$

476 The scaling factor,  $\alpha \in [0,1]$ , controls the reduction in effective axial drag coefficient for the low-frequency velocity  
477 components.

478 With the introduction of the high-pass filter, two additional tunable model parameters are introduced: the cutoff  
479 frequency,  $f_c$ , and the scaling factor,  $\alpha$ , for the axial drag coefficient. In the present investigation,  $f_c$  is always set to  
480 0.07 Hz, just below the wave peak frequency of 0.083 Hz. The scaling factor  $\alpha$  was set to 0.5 as an initial guess,  
481 which produced good predictions; therefore, no further tuning was performed. The axial drag coefficient,  $C_{D_{Ax}}$ , was  
482 kept as 4.1 as in the original model in Section 3.1. One drawback of the current approach is that, strictly speaking,  
483 some a priori knowledge of the motion response of the structure from either wave-basin experiments or CFD  
484 simulations is required to tune the scaling factor,  $\alpha$ .

485 With this final modification to the OpenFAST model, the PSDs of the predicted heave and pitch motions of the  
486 structure in irregular waves (LC 5.3) are shown in Figure 16. The experimental measurements and the predictions by  
487 the original model of Robertson et al. [9] are both included for reference. The corresponding PSD integrals are  
488 shown in Figure 17. The addition of the high-pass filter leads to good agreement between the present modified  
489 OpenFAST model and the experiment for both the heave resonance motion and the low-frequency pitch resonance  
490 motion (for comparison, see Figure 14 for the results without the high-pass filter). Note that without the additional  
491 global linear damping in pitch of 31 MN·m·s/rad discussed in Section 3.1, the prediction of the low-frequency pitch  
492 PSD integral by the present modified OpenFAST model will increase slightly by approximately 8%, which  
493 corresponds to a 4% increase in the pitch resonance amplitude. The added damping has a negligible effect on the  
494 wave-frequency pitch response.

495 The heave resonance peak frequency is slightly shifted in the model prediction compared to the experiment  
496 because the actual heave added mass is slightly higher than the linear potential-flow prediction owing to viscous  
497 effects (recently confirmed for this exact floater geometry using CFD simulations [34]). This effect tends to be more  
498 significant for flat-bottomed bodies [35] and can be corrected by simply applying a scaling factor for the potential-  
499 flow added mass [36], which was not done for the present results. The floater motion near the wave peak frequency  
500 of 0.083 Hz remains unaffected. It is possible that a more sophisticated filter design can lead to further improved  
501 agreement between the model and the experiment across all frequency ranges; however, the current simple filter is  
502 considered adequate while having the benefit of keeping the number of tunable parameters to a minimum.

503 Note that the addition of the filter has practically no effect on the wave excitation in surge on the structure  
 504 under a fixed condition or on the prediction of surge motion; both remain in good agreement with the experiment as  
 505 shown in Section 4.1. The effects of using the filtered velocity on the pitch moment on the structure under the fixed  
 506 condition are illustrated in Figure 18. The PSDs of the pitch moment obtained with Eq. (5) and Eq. (8) are very  
 507 similar, as shown in Figure 18a; using the filtered velocity slightly reduces the low-frequency PSD integral of the  
 508 pitch moment (Figure 18b), resulting in slightly improved agreement with the experiment given the same value of  
 509  $C_{D_{Ax}}$  of 4.1.

510 The comparison of heave force on the fixed structure is shown in Figure 19. Overall, the modified model with  
 511 Eq. (8) for heave-plate drag produces improved predictions of the low-frequency heave force above 0.02 Hz and of  
 512 the wave-frequency force below 0.07 Hz (see Figure 19a); however, a slight overprediction near the surge resonance  
 513 frequency of 0.01 Hz is also observed with both Eq. (5) and Eq. (8). The use of the filtered velocity in Eq. (8)  
 514 alleviates this overprediction, resulting in better agreement with the experiment in terms of the low-frequency PSD  
 515 integral of the heave force compared to using Eq. (5). Either way, the low-frequency heave excitation is of little  
 516 engineering importance because the heave resonance frequency of this structure is much higher at around 0.58 Hz  
 517 and is excited by the stronger direct wave-frequency excitation. All OpenFAST models predict approximately the  
 518 same wave-frequency heave excitation.

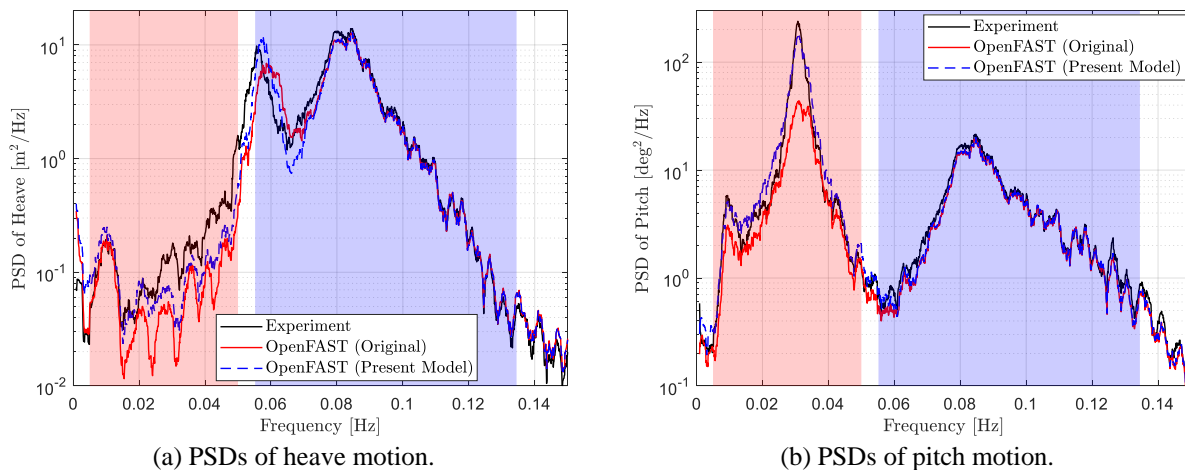


**Figure 16.** PSDs of (a) heave motion and (b) pitch motion of the freely floating offshore wind semisubmersible in irregular waves (LC 5.3). With the presentFAST model, the axial drag was computed using Eq. (8). The pink region indicates the low-frequency range, and the blue region is the wave-frequency range (see Table 2). For comparison, the pitch motion predicted without the filtered velocity using Eq. (5) is shown in Figure 14.

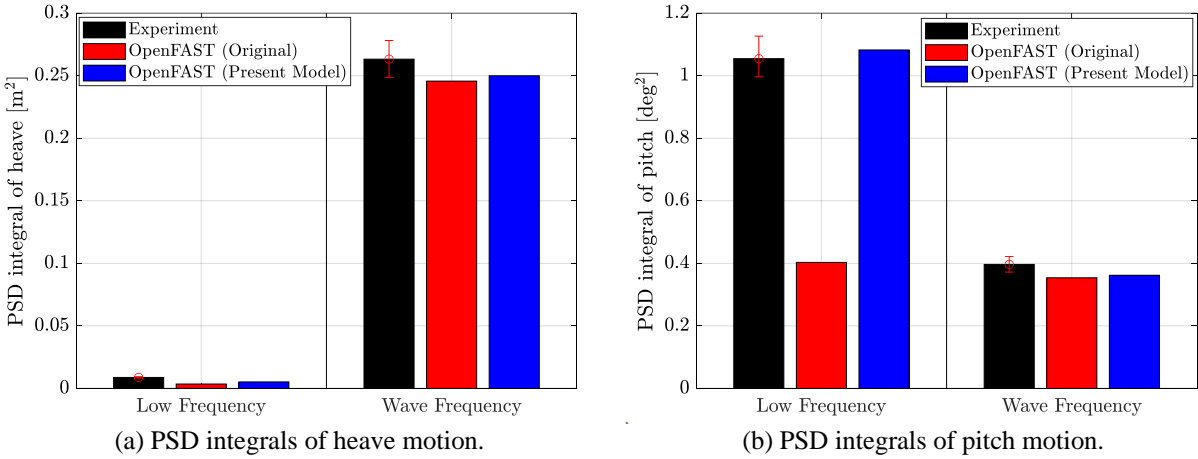


**Figure 17.** PSD integrals of (a) heave motion and (b) pitch motion of the freely floating offshore wind semisubmersible in irregular waves (LC 5.3). With the present model, the axial drag was computed using Eq. (8).

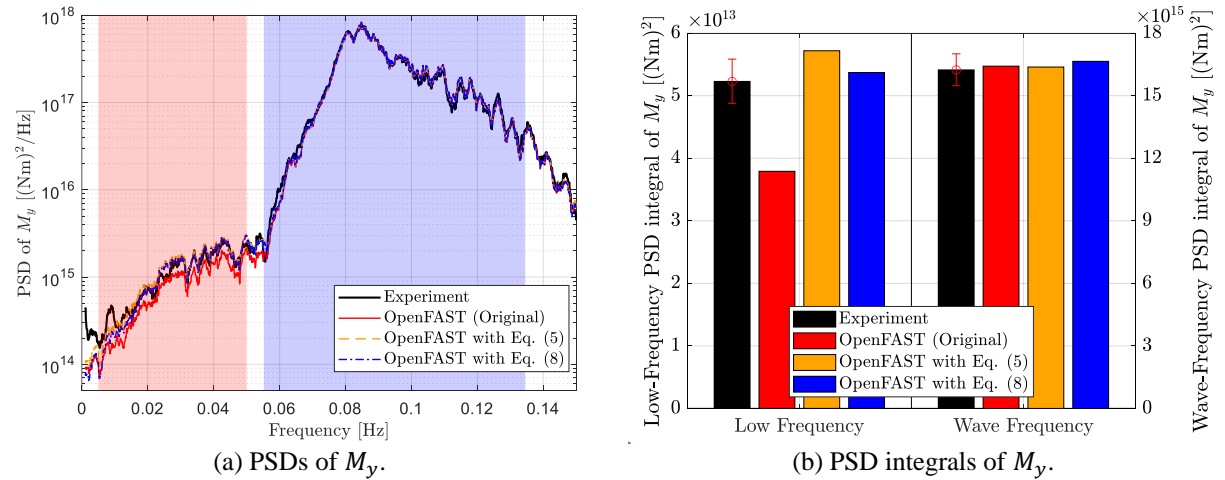


**Figure 18.** Comparisons of (a) PSD and (b) PSD integrals of the pitch moment on the fixed offshore wind semisubmersible in irregular waves (LC 3.3) predicted using Eq. (5) (without filtered velocity) and Eq. (8) (with filtered velocity) for the axial heave-plate drag force. The pink region indicates the low-frequency range, and the blue region is the wave-frequency range (see Table 2). The original OpenFAST model of [9] is described in Section 3.1.

521 Finally, we emphasize that the robust modeling of drag force in complex flow environments remains an open  
 522 question. Although we have strived to provide physical justifications of using a high-pass-filtered relative velocity in  
 523 the computation of heave-plate drag force, the proposed model is still a heavily simplified and approximate one  
 524 based more on empirical observation of the experimental measurements. The model obviously does not capture the  
 525 highly complex flow behavior near the corners of the heave plates; however, at the same time, it is apparent that the

526 proposed drag formulation improved the model predictions of not just the pitch motion under a floating condition  
 527 but also the heave force on the fixed structure for the wave conditions investigated in this article with no detrimental  
 528 side effects on the prediction of other metrics (also, see Section 5). Further investigation is needed to better establish  
 529 the validity and the range of applicability of the proposed formulation with the filtered velocity.

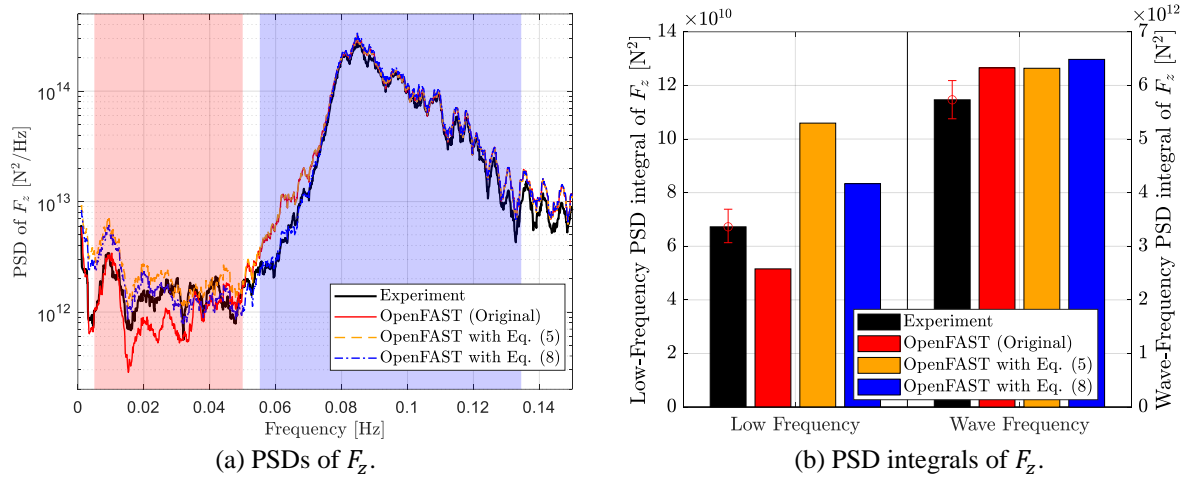


**Figure 19.** Comparisons of (a) PSD and (b) PSD integrals of the heave force on the fixed offshore wind semisubmersible in irregular waves (LC 3.3) predicted using Eq. (5) (without filtered velocity) and Eq. (8) (with filtered velocity) for the axial heave-plate drag force. The pink region indicates the low-frequency range, and the blue region is the wave-frequency range (see Table 2). The original OpenFAST model of [9] is described in Section 3.1.

530

#### 531 4.4 Summary of all modifications to the OpenFAST model

532 All modifications to the OpenFAST model described in Section 4 are made with respect to the drag force, both  
 533 transverse and axial. The changes and the model coefficients used are summarized in Table 3. Overall, the present  
 534 model has succeeded, at least for the load cases considered, in the task of accurately capturing the surge and pitch  
 535 resonance excited by the nonlinear, low-frequency wave excitation. As discussed previously, this is a nontrivial task  
 536 as indicated by the recent studies of Robertson et al. [1,9], which showed that most state-of-the-art engineering  
 537 models for floating offshore wind turbines severely underestimate both low-frequency excitation on a fixed platform  
 538 and the corresponding motion response of a floating platform. Furthermore, the current approach reconciles the  
 539 fixed condition and the floating condition by obtaining good predictions for both using a single unified model with  
 540 the same set of coefficients.

541

542 **Table 3.** Summary of the proposed modifications to the OpenFAST model for improved low-frequency predictions.

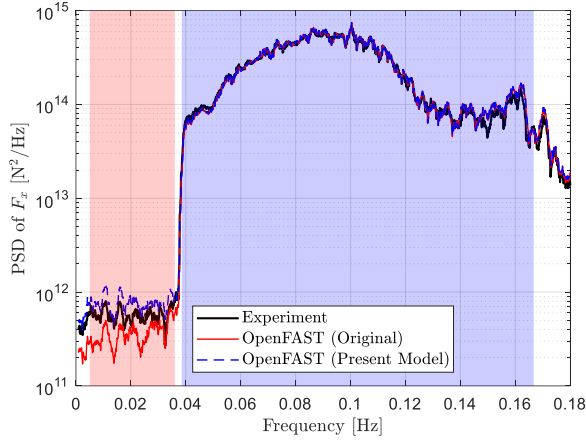
	Original OC6 Model	Present Modified Model	Effects
Transverse drag	Uniform $C_D = 0.4$ on the upper columns and the main column.	$C_D = 1.6$ near the waterline. $C_D = 0.4$ on the submerged section of the upper columns and the main column.	Improves the prediction of low-frequency surge force on the fixed structure and surge motion of the floating structure.
Heave-plate axial/normal drag	Axial drag force evaluated and applied at both faces (top and bottom) of the heave plates. Eq. (2) with $C_{D_{Ax}} = 4.1$ .	Axial drag force only evaluated and applied at the face with $v_{r,n} > 0$ , meaning the normal flow points away from the heave plate. Part of the drag computed from high-pass-filtered relative normal flow velocity. Eq. (8) with $C_{D_{Ax}} = 4.1$ .	Evaluating the axial drag force only on the face with $v_{r,n} > 0$ improves the prediction of low-frequency pitch moment on a fixed structure. Computing part of the drag force using high-pass-filtered relative normal flow velocity improves the prediction of low-frequency pitch resonance.

### 543 **5 Blind validation of the modified model with white-noise waves**

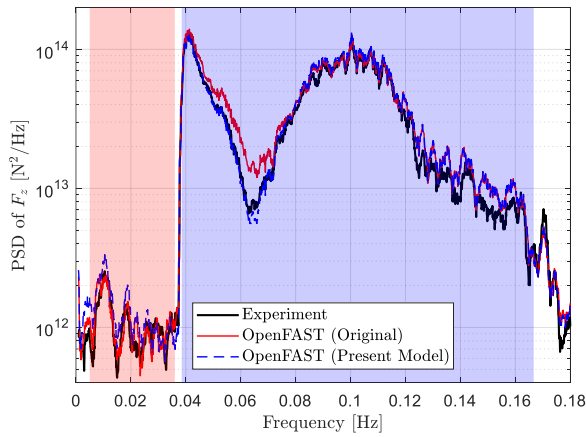
544 Using the modified OpenFAST model, the hydrodynamic forces on the OC6-DeepCwind semisubmersible  
 545 when fixed and the motion response while freely floating in the white-noise waves (LC 3.4 and LC 5.4, respectively,  
 546 in Table 2) were also computed as an additional blind validation. Although we had access to the experimental results  
 547 for the white-noise waves beforehand, these data were not referenced when tuning the model parameters.

548 The wave loads on the fixed semisubmersible are shown in Figure 20 (LC 3.4). Compared to the original model,  
 549 the present modified model predicts higher low-frequency surge force because of the increased drag coefficient near  
 550 the waterline. As shown in Figure 20a, the low-frequency surge force from the present model appears to be more  
 551 consistent with the experiment; however, the PSD integrals shown in Figure 20d suggest the present model  
 552 overpredicts the low-frequency surge excitation, whereas the original model underpredicts. It is likely that much  
 553 better agreement with the experiment in the low-frequency surge excitation can be achieved with the present model  
 554 by slightly reducing the transverse drag coefficient near the waterline; however, this was not done, in the spirit of  
 555 blind validation.

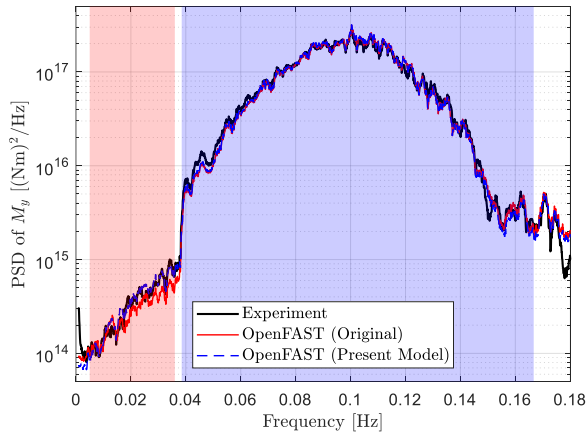
556 In Figure 20b and Figure 20e, both OpenFAST models produce similar predictions for the heave force, with the  
 557 present model showing slightly better agreement with the experiment over the wave-frequency range. The present  
 558 model also provides an improved prediction of the low-frequency pitch moment compared to the original model  
 559 with the modified formulation of the heave-plate axial drag force of Eq. (8).



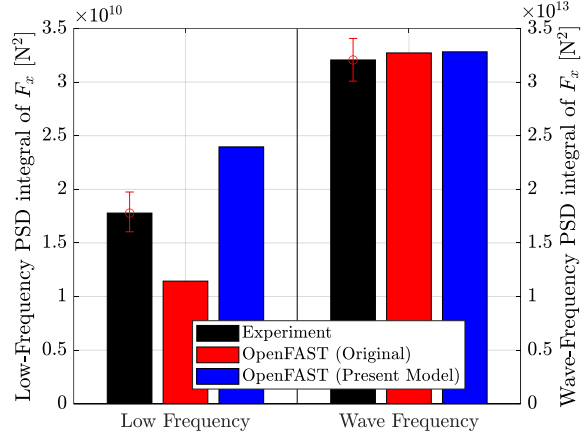
(a) PSDs of  $F_x$ .



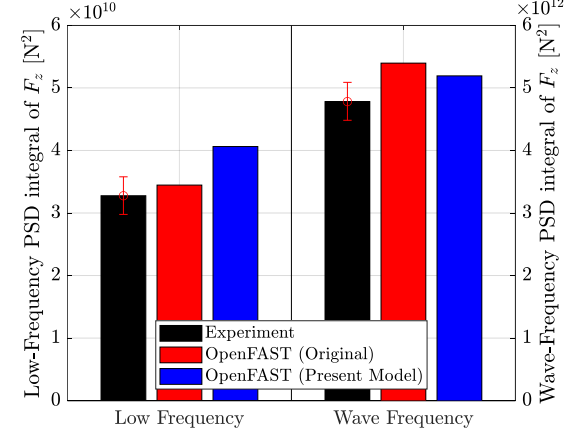
(b) PSDs of  $F_z$ .



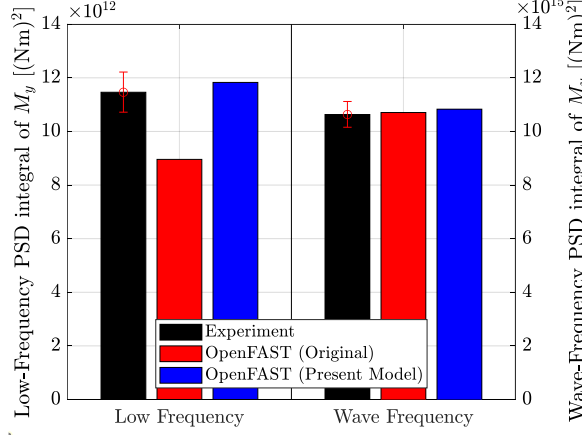
(c) PSDs of  $M_y$ .



(d) PSD integrals of  $F_x$ .

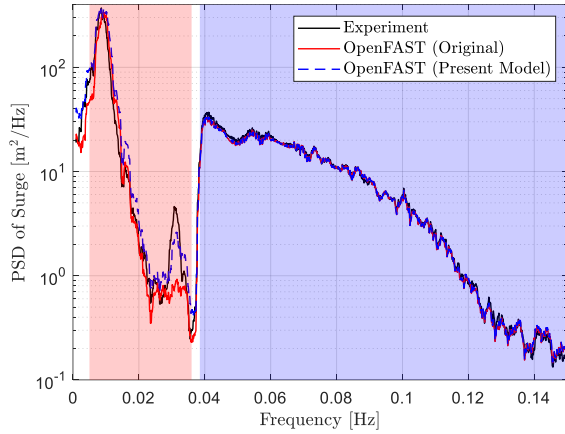


(e) PSD integrals of  $F_z$ .

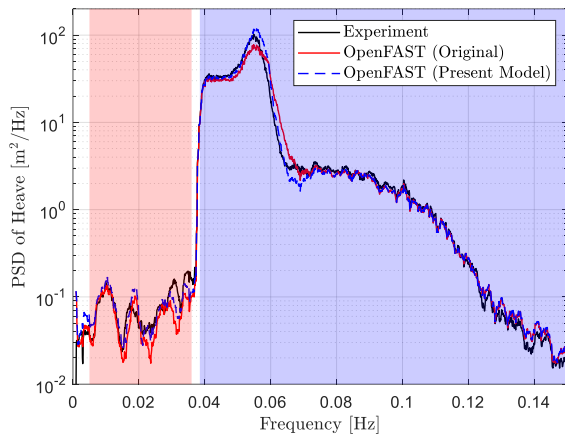


(f) PSD integrals of  $M_y$ .

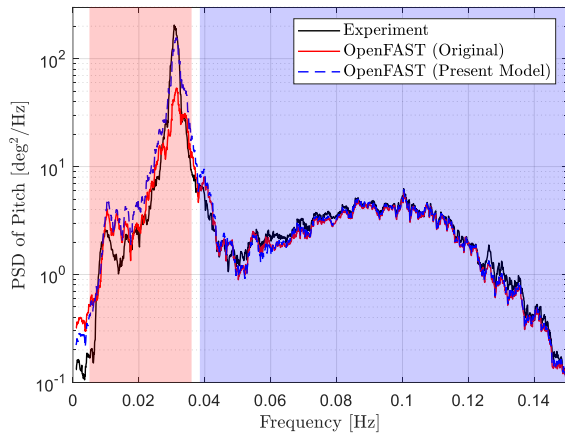
**Figure 20.** PSDs of wave-induced (a) surge force, (b) heave force, and (c) pitch moment on the fixed offshore wind semisubmersible in the white-noise waves (LC 3.4), and (d–f) the corresponding PSD integrals. In (a–c), the pink region indicates the low-frequency range, and the blue region is the wave-frequency range (see Table 2).



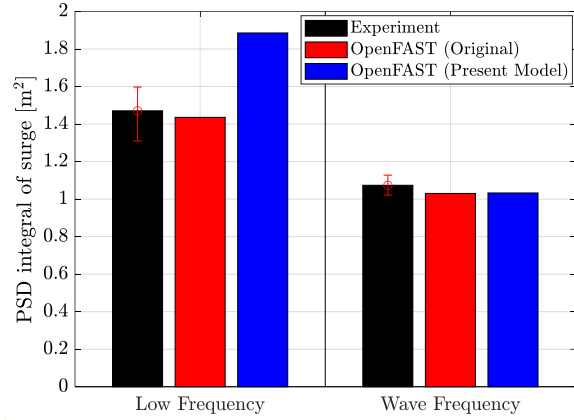
(a) PSDs of surge motion.



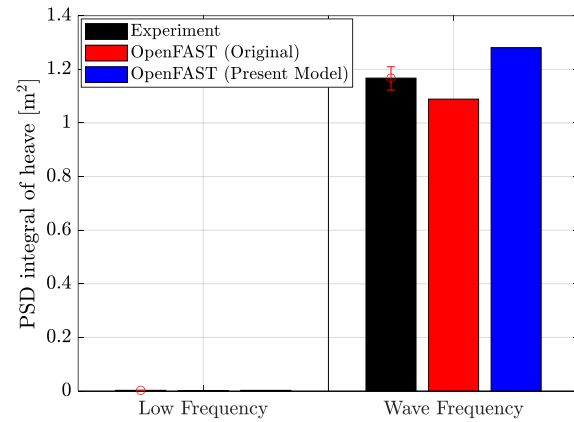
(b) PSDs of heave motion.



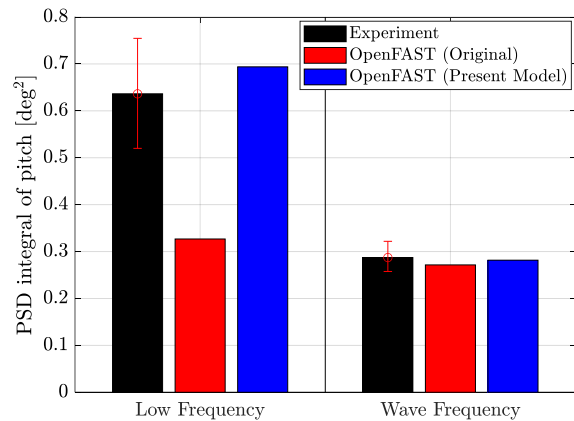
(c) PSDs of pitch motion.



(d) PSD integrals of surge motion.



(e) PSD integrals of heave motion.



(f) PSD integrals of pitch motion.

**Figure 21.** PSDs of wave-excited (a) surge motion, (b) heave motion, and (c) pitch motion of the freely floating offshore wind semisubmersible in the white-noise waves (LC 5.4), and (d–f) the corresponding PSD integrals. In (a–c), the pink region indicates the low-frequency range, and the blue region is the wave-frequency range (see Table 2).

562 The motion of the semisubmersible when freely floating in white-noise waves (LC 5.4) is shown in Figure 21.  
563 The low-frequency surge resonance motion is slightly overpredicted by the present model as shown in Figure 21d,  
564 whereas the original model shows better agreement with the experiment. This is likely caused by the overprediction  
565 of the low-frequency surge force shown in Figure 20a and Figure 20d. The two OpenFAST models both show  
566 reasonably good agreement with the experiment in terms of the wave-frequency heave-motion PSD integral in  
567 Figure 21e, with one underpredicting and the other slightly overpredicting. The most significant improvement with  
568 the present model is in the prediction of the low-frequency pitch resonance motion shown in Figure 21c and Figure  
569 21f. The pitch resonance is severely underpredicted by the original model, whereas the present model shows very  
570 good agreement with the experiment in terms of the low-frequency pitch-motion PSD integral.

571 Overall, the present modified model gives reasonable predictions, for the white-noise waves, of both the wave  
572 excitation on the fixed structure and the motion of the floating structure in both low-frequency and wave-frequency  
573 ranges without any retuning. This suggests that the modified model is reasonably general with regard to the input  
574 waves and should provide adequate predictions for a range of wave conditions. This is, of course, a highly valuable  
575 feature in engineering models for design purposes. With the white-noise waves, the most significant improvements  
576 compared to the original model are in the low-frequency pitch moment and pitch motion, whereas the improvements  
577 to low-frequency surge force and motion are not as obvious as with the irregular-wave condition of LC 3.3 and LC  
578 5.3; however, it should be emphasized that the wide-band white-noise sea state is rather unrealistic, and we believe  
579 that with a minimal amount of tuning, the present model can still provide improved predictions in surge when  
580 dealing with more realistic narrow-banded sea states, as demonstrated with LC 3.3 and LC 5.3 in Section 4.

## 581 **6 Discussions and recommendations for future applications**

582 Similar to the QTF-correction method of Li and Bachynski-Polić [21], the modifications to the empirical drag  
583 forces presented in the current article are aimed at providing candidate solutions to the underprediction of the low-  
584 frequency wave excitation and responses of floating wind semisubmersibles by mid-fidelity engineering models  
585 [1,9], a common issue encountered not just with the DeepCwind semisubmersible investigated here but also with  
586 many other floater designs (e.g., [2,3,15]); however, the philosophies behind the present approach and that of [21]  
587 are very different.

588 The method of correcting the QTFs from second-order potential-flow theory is based on leveraging the CFD  
589 solutions as much as possible in a quantified fashion. The results from many CFD simulations spanning a range of  
590 frequencies are used to modify the QTFs; therefore, it can be expected that this method will yield accurate  
591 predictions of the nonlinear, difference-frequency wave loads for a wide range of wave frequencies, at least for a  
592 fixed structure and when the wave amplitudes are similar to those used in the CFD simulations. This method is more  
593 numerical in nature.

594 In the present work, we attempted to identify the underlying physical mechanisms that are missing in the mid-  
595 fidelity models that are causing the underprediction, and we proposed modifications to the empirical drag forces  
596 based on general physical arguments aimed at addressing the identified deficiencies. We also strived to make the  
597 modifications as simple as possible and introduce minimal additional tunable parameters. It is our hope that the  
598 proposed solution can be more easily applied in practice.

599 The QTF-correction method [21] was demonstrated to be highly effective in improving the low-frequency  
600 predictions; however, there remain some open questions and limitations, which we hope to circumvent with the  
601 alternative approach proposed in this article.

602 First, a proper application of the QTF-correction method requires many bichromatic-wave CFD simulations,  
603 which need to be repeated whenever the design changes. To some extent, this requirement negates the advantage of  
604 mid-fidelity models in design optimization. The correction of the QTFs (both magnitude and phase), which depends  
605 on two frequencies, is also not trivial. In Ref. [21], the possible frequency pairs over the frequency range of interest  
606 were mapped into different regions, and, over each region, different assumptions were made about the corrected  
607 QTF values to facilitate the correction based on the available CFD results. It is unclear whether the proposed  
608 mapping and the associated assumptions about the QTFs are generally applicable to different floater geometries. The  
609 alternative method documented in the present article, on the other hand, does not require as many CFD simulations  
610 to tune the few additional model parameters. Of course, some a priori information is still required to tune the model  
611 as with any mid-fidelity approach. For instance, the nonlinear, low-frequency surge force is primarily controlled by  
612 just one parameter, the increased drag coefficient near the waterline, which can be determined from just a few sets of  
613 CFD simulations or experimental measurements. The modification to the axial drag force on the heave plates that  
614 improves the low-frequency pitch moment introduces no new parameters that require tuning. The drawback of the

615 present method compared to the QTF-correction approach is that the range of frequencies over which the predictions  
616 of the nonlinear, low-frequency wave loads remain accurate is not as obvious.

617 Second, the nonlinear, low-frequency excitation might not always be quadratic in nature. For instance, the  
618 present work suggests that the viscous drag force near the waterline, in conjunction with wave stretching, is the  
619 dominant contributor to the low-frequency surge excitation. This is a third-order effect; therefore, the method of  
620 modifying the QTFs might lead to errors when the wave amplitudes are different from those used in the CFD  
621 simulations, because this method forces the correction to the low-frequency excitation to scale quadratically with  
622 wave amplitude. In the present work, we hope that by identifying the underlying physical cause of the  
623 underprediction, the results will scale more appropriately with the incident wave amplitudes, at least within a  
624 moderate range.

625 Finally, application of the QTF-correction method to a floating structure requires the assumption that the same  
626 corrections to the QTFs determined from the CFD simulations of a restrained structure in bichromatic waves (i.e.,  
627 the differences between the QTFs for a fixed structure estimated from the CFD simulations and from the second-  
628 order potential-flow theory) remain valid and can be used to directly modify the QTFs of a floating structure from  
629 potential-flow theory [22]. This assumption requires further investigation, especially when viscous drag plays a  
630 major role in the nonlinear low-frequency excitation. In contrast, the modifications to the Morison drag forces  
631 proposed in the present work should be equally applicable to a fixed structure and a moving structure when the  
632 relative flow velocity is used.

633 Overall, both the present approach and the QTF-correction method [21] provide significantly improved  
634 predictions of the low-frequency wave excitation and responses of a floating wind semisubmersible for the wave  
635 conditions and floater geometry investigated. At the same time, both leave some open questions as to their  
636 applicability to changes in wave conditions and floater geometries. The modeling techniques proposed in this article,  
637 developed based on a different philosophy, represent a possible alternative to the QTF-correction method [21].

638 Although the underprediction of the low-frequency resonance responses of floating wind semisubmersibles is a  
639 common issue, the modifications to the OpenFAST model presented in this article are specifically devised with the  
640 OC6-DeepCwind semisubmersible in mind, for which we have limited but high-quality experimental measurements.  
641 Without access to good-quality experimental data for other floater designs, it is difficult to draw any definitive  
642 conclusion on the applicability of the proposed changes to the OpenFAST model to other floater geometries.

643 Nevertheless, based on the physical arguments behind the modifications, we conjecture the following guidance for  
644 future applications to other floater designs:

- 645 1) We believe an increased transverse drag coefficient near the waterline (discussed in Section 4.1) should be  
646 used for vertical surface-piercing circular columns whenever low-frequency surge resonance is of concern.  
647 The increase in effective drag coefficient near the waterline has been observed in prior studies for a single  
648 circular cylinder in isolation in both current [30] and wave conditions [31] and is likely a common  
649 phenomenon; however, the drag coefficient near the waterline will likely have to be tuned to some degree if  
650 vastly different wave conditions are considered. The use of increased waterline drag coefficients for  
651 surface-piercing columns of different cross sections, such as a square column, requires further  
652 investigation. In this case, the drag coefficient will also strongly depend on the wave direction, which is not  
653 considered in the present investigation.
- 654 2) As discussed in Section 4.2, the modification to the axial drag coefficient on the heave plates, which limits  
655 the drag force to the face with  $v_{r,n} > 0$  (normal flow velocity pointing away from the face) is only required  
656 when the floater design incorporates thick heave plates like the DeepCwind semisubmersible. If the low-  
657 frequency pitch moment is underpredicted, this modification will likely improve the results. For thin heave  
658 plates, this modification will not have a significant impact; however, if the diameter of the heave plate  
659 relative to the diameter of the upper column is close to unity, the modified formulation of Eq. (5) can still  
660 be used to prescribe different drag coefficients depending on the flow direction to reflect the asymmetry  
661 about the heave-plate plane. This is not explored in the present study because of the large heave-plate  
662 diameter relative to the column diameter (see Section 4.2).
- 663 3) The high-pass filtering of the normal relative flow velocity when computing the heave-plate drag force  
664 discussed in Section 4.3 is also based on the general physical argument that the vortex shedding at the  
665 corners of the heave plates is mostly controlled by the more rapid wave-frequency flow and body  
666 oscillation rather than the body motion at the low pitch resonance frequency. As a result, the drag force  
667 would be more closely linked to the wave-frequency velocity components and would react less to the low-  
668 frequency velocity components. We believe this velocity filtering is generally applicable to  
669 semisubmersible designs with heave plates and with a pitch resonance frequency below the wave-frequency

670 range; however, the filter parameters will require some tuning based on the specific floater design and the  
671 incident wave peak frequency.

672 Inevitably, mid-fidelity hydrodynamic modeling based on potential-flow theory and empirical drag forces needs  
673 to be tailored and tuned to some degree to the specific floater design and wave conditions being analyzed. Rather  
674 than developing a model that works for all semisubmersible designs and wave conditions automatically, which is not  
675 possible in our opinion, the intention of the present work is to suggest several simple yet physically justifiable  
676 modifications to the hydrodynamic modeling of offshore wind semisubmersibles that could potentially lead to  
677 significant improvements in the model predictions should future modelers also encounter difficulties with the low-  
678 frequency nonlinear load and responses. If and which modifications are needed should be decided at the discretion  
679 of future modelers depending on the specific floater design and wave conditions.

## 680 **7 Conclusions**

681 In the previous OC5 project and the ongoing OC6 project, the state-of-the-art, mid-fidelity engineering-level  
682 tools for floating offshore wind turbines were found to consistently underpredict the low-frequency responses of  
683 semisubmersible offshore wind platforms, both loads and motion. To address this deficiency, a modified OpenFAST  
684 model was developed in the present article as a major outcome of the OC6 Phase I investigation, which involved a  
685 three-way validation study with mid-fidelity engineering-level tools, high-fidelity CFD simulations, and wave-basin  
686 experiments into the low-frequency responses of offshore wind semisubmersibles.

687 Throughout this study, the open-source OC6-DeepCwind semisubmersible offshore wind platform was adopted  
688 as a generic design. Four load cases from the OC6 Phase I investigation were used: 3.3, 3.4, 5.3, and 5.4. LC 3.3 and  
689 LC 5.3 have the same JONSWAP incident wave spectrum, with LC 3.3 having a fixed platform and LC 5.3 a freely  
690 floating platform. LC 3.4 and LC 5.4 both have the same white-noise incident waves, with LC 3.4 corresponding to  
691 a fixed condition and LC 5.4 a freely floating condition. Experimental measurements for all four load cases are  
692 available from the OC6 Phase I experimental validation campaign. The experimentally measured wave forces and  
693 moments from LC 3.3 and the floater pitch motion from LC 5.3 were used to tune the modified OpenFAST model;  
694 the measured forces and moments from LC 3.4 as well as the measured motion responses from LC 5.4 were reserved  
695 for a blind validation and were not referenced during model tuning.

696 Based on the data gathered from the OC6 Phase I project, we proposed three changes to the OpenFAST model  
697 formulation and modeling practice that improve the predictions of the low-frequency responses without significantly  
698 increasing the difficulty of model parameter tuning. The number of tunable model parameters was deliberately kept  
699 low to avoid overfitting.

700 First, we identified the transverse viscous drag force on the vertical columns near the waterline to be the  
701 primary contributor to the nonlinear, low-frequency surge force near the very low surge resonance frequency. In  
702 contrast, second-order wave diffraction has a negligible contribution in this frequency range. This is consistent with  
703 the observation made during the CFD investigation of OC6 Phase I. We therefore proposed the use of an increased  
704 transverse drag coefficient in the region near the free surface in conjunction with vertical wave stretching. At the  
705 same time, to avoid excessive surge damping under a freely floating condition, a lower transverse drag coefficient  
706 previously tuned against free-decay and forced-oscillation experiments was used for the submerged section of the  
707 columns. This use of a depth-dependent drag coefficient led to excellent agreement with the experiment in the wave  
708 surge force throughout the entire low-frequency range for LC 3.3 and in the low-frequency surge resonance motion  
709 for LC 5.3.

710 Second, we modified the formulation of the axial/normal viscous drag on the faces of the heave plates. In the  
711 original model, the axial drag force is simultaneously applied to the face toward and away from the flow. Whereas  
712 this is an appropriate formulation for bodies that are modeled with the Morison equation only, it is not entirely  
713 suitable for members already modeled by potential flow, like the heave plates, because the increased pressure on the  
714 face toward which the flow is directed is already accounted for in the potential-flow solution. We therefore modified  
715 the OpenFAST model to only evaluate and apply the axial drag force on the face from which the flow is directed  
716 away to account for the effect of flow separation. Although this modification has negligible effects for thin heave  
717 plates, the OC6-DeepCwind floater incorporates thick heave plates with nonnegligible variation of the incident  
718 wave-field velocity with depth across the height of the heave plates; this modification led to much better agreement  
719 with the experiment in the low-frequency pitch moment on the fixed platform for both LC 3.3 and LC 3.4.

720 Finally, by inspecting the effects of the axial drag coefficient for the heave plates on the heave and pitch motion  
721 of the structure, it was observed that a lower drag coefficient improved the agreement between the model prediction  
722 and the experiment in the low-frequency range near pitch resonance, whereas an increased drag coefficient  
723 improved the agreement at higher frequencies. It is, however, difficult to implement frequency-dependent drag

724 coefficients in a time-domain model like OpenFAST; therefore, a simplified approach was proposed in which part of  
725 the axial drag force is calculated based on a high-pass-filtered relative normal flow velocity. This modification led to  
726 good agreement between the model and the experiment in both the low-frequency pitch resonance motion and the  
727 wave-frequency heave resonance motion for both LC 5.3 and LC 5.4.

728 Overall, the new unified model with a single set of coefficients presented in this article simultaneously provides  
729 good predictions of the nonlinear, low-frequency excitation on a fixed offshore wind semisubmersible and the  
730 resonance motions in surge and pitch of the same structure when freely floating. For LC 3.3, the nonlinear, low-  
731 frequency wave surge force and pitch moment on the fixed structure predicted by the new modified OpenFAST  
732 model are within a 7% and 3% difference from the experimental measurements, respectively, in terms of the low-  
733 frequency PSD integrals. In comparison, the original OpenFAST model developed for the OC5/6 projects  
734 underpredicts the low-frequency surge force and pitch moment by 52% and 27%, respectively. With LC 5.3, the  
735 low-frequency surge and pitch resonance motions of the freely floating structure predicted by the new model are  
736 both within a 3% difference from the experimental measurements, showing a significant improvement from the  
737 original model, which underpredicts the surge and pitch resonance by 47% and 62%, respectively. With the blind  
738 validation using a white-noise wave (LC 3.4 and LC 5.4), the new model overpredicts the low-frequency surge force  
739 on the fixed structure by 35% and the surge resonance motion of the floating structure by 30%. In contrast, the  
740 original model underpredicts the low-frequency surge force by 36% but shows good agreement with the experiment  
741 in terms of the surge resonance motion with only a 3% difference. We consider the predictions by the new model  
742 acceptable, and it is very likely that they will be improved if the transverse drag coefficient near the waterline is  
743 slightly reduced, which was not done, in the spirit of a blind validation. With pitch, however, the new model shows  
744 significant improvements over the original model. The low-frequency pitch moment, previously underpredicted by  
745 22% by the original model, is now within a 4% difference of the experiment with the new model. The improvement  
746 in the prediction of the low-frequency pitch motion is more significant with the original model underpredicting by  
747 49% and the new model giving a prediction within a 10% difference from the experiment. This improvement is  
748 achieved without having to retune the model parameters for the white-noise wave condition. Both the original and  
749 the new model give similar predictions for the wave-frequency loads and motion responses that are consistent with  
750 the experimental measurements.

751 The new model only introduces three new tunable parameters: the increased transverse drag coefficient near the  
752 waterline, the cutoff frequency of the high-pass velocity filter for computing the axial drag, and a scaling factor for  
753 the axial drag coefficient at low frequencies. As with any mid-fidelity model, some a priori information on the  
754 hydrodynamic characteristics of the floater from either experiments or high-fidelity CFD simulations is needed for  
755 model tuning; however, the fact that the model provides good predictions for the floater in white-noise waves  
756 without being specifically tuned for this condition demonstrates a degree of generalness of the model coefficients.  
757 We believe this is a nontrivial improvement over the existing mid-fidelity models used in the OC6 Phase I  
758 investigation, which, in general, were not able to match all low-frequency responses from the experiment at the  
759 same time. After further verification and validation, we plan to implement the proposed changes in a future version  
760 of OpenFAST as optional features to support the design and optimization of floating offshore wind platforms.

## 761 **Acknowledgements**

762 This work was authored by the National Renewable Energy Laboratory, operated by Alliance for Sustainable  
763 Energy, LLC, for the U.S. Department of Energy (DOE) under Contract No. DE-AC36-08GO28308. Funding  
764 provided by the U.S. Department of Energy Office of Energy Efficiency and Renewable Energy Wind Energy  
765 Technologies Office. The views expressed in the article do not necessarily represent the views of the DOE or the  
766 U.S. Government. The U.S. Government retains and the publisher, by accepting the article for publication,  
767 acknowledges that the U.S. Government retains a nonexclusive, paid-up, irrevocable, worldwide license to publish  
768 or reproduce the published form of this work, or allow others to do so, for U.S. Government purposes.

## 769 **References**

- 771 [1] A.N. Robertson, F. Wendt, J.M. Jonkman, W. Popko, H. Dagher, S. Gueydon, J. Qvist, F. Vittori, J. Azcona, E.  
772 Uzunoglu, et al., OC5 Project Phase II: Validation of global loads of the DeepCwind floating semisubmersible  
773 wind turbine, *Energy Procedia* 137 (2017) 38–57. <https://doi.org/10.1016/j.egypro.2017.10.333>.
- 774 [2] L.H.S. do Carmo, P.C. de Mello, E.B. Malta, G.R. Franzini, A.N. Simos, R.T. Gonçalves, H. Suzuki, Analysis  
775 of a FOWT model in bichromatic waves: an investigation on the effect of combined wave-frequency and slow  
776 motions on the calibration of drag and inertial force coefficients. In: *ASME 39th International Conference on*  
777 *Ocean, Offshore and Arctic Engineering*; 2020. <https://doi.org/10.1115/OMAE2020-18239>.
- 778 [3] C. Lopez-Pavon, R.A. Watai, F. Ruggeri, A.N. Simos, A. Souto-Iglesias, 2015. Influence of wave induced  
779 second-order forces in semisubmersible FOWT mooring design. *J. Offshore. Mech. Arct. Eng.* 137(3), 031602.  
780 <https://doi.org/10.1115/1.4030241>.
- 781 [4] F. Caillé, P. Bozonnet, T. Perdrizet, Y. Poirrette, C. Melis, Model test and simulation comparison for an  
782 inclined-leg TLP dedicated to floating wind. In: *ASME 36th International Conference on Ocean, Offshore and*  
783 *Arctic Engineering*; 2017. <https://doi.org/10.1115/OMAE2017-61652>.

- 784 [5] J. Azcona, F. Bouchotrouch, F. Vittori, Low-frequency dynamics of a floating wind turbine in wave tank-scaled  
785 experiments with SiL hybrid method, *Wind Energy* 22 (2019) 1402–1413. <https://doi.org/10.1002/we.2377>.
- 786 [6] A. Robertson, E.E. Bachynski, S. Gueydon, F. Wendt, P. Schünemann, 2020. Total experimental uncertainty in  
787 hydrodynamic testing of a semisubmersible wind turbine, considering numerical propagation of systematic  
788 uncertainty. *Ocean Eng.* 195, 106605. <https://doi.org/10.1016/j.oceaneng.2019.106605>.
- 789 [7] M. Fowler, 1/50-scale DeepCwind semi-submersible component wave testing, University of Maine, Advanced  
790 Structures and Composites Center, Orono, Maine, USA, 2021.
- 791 [8] A. Robertson, L. Wang, 2021, OC6 Phase Ib: Floating wind component experiment for difference-frequency  
792 hydrodynamic load validation. *Energies* 14(19), 6417. <https://doi.org/10.3390/en14196417>.
- 793 [9] A.N. Robertson, S. Gueydon, E. Bachynski, L. Wang, J. Jonkman, D. Alarcón, E. Amet, A. Beardsell, P.  
794 Bonnet, B. Boudet, et al., 2020. OC6 Phase I: Investigating the underprediction of low-frequency hydrodynamic  
795 loads and responses of a floating wind turbine. *J. Phys.: Conf. Ser.* 1618(3), 032033.  
796 <https://doi.org/10.1088/1742-6596/1618/3/032033>.
- 797 [10] L. Wang, A. Robertson, J. Jonkman, Y.-H. Yu, 2021. Uncertainty assessment of CFD investigation of the  
798 nonlinear difference-frequency wave loads on a semisubmersible FOWT platform. *Sustainability* 13(1), 64.  
799 <https://doi.org/10.3390/su13010064>.
- 800 [11] L. Wang, A. Robertson, J. Jonkman, Y.-H. Yu, A. Koop, A. Borràs Nadal, H. Li, W. Shi, R. Pinguet, Y. Zhou,  
801 Q. Xiao, R. Kumar, H. Sarlak, Investigation of nonlinear difference-frequency wave excitation on a  
802 semisubmersible offshore-wind platform with bichromatic-wave CFD simulations. In: *ASME 3rd International*  
803 *Offshore Wind Technical Conference*; 2021. <https://doi.org/10.1115/IOWTC2021-3537>.
- 804 [12] L. Wang, A. Robertson, J. Jonkman, Y.-H. Yu, A. Koop, A. Borràs Nadal, H. Li, E. Bachynski-Polić, R.  
805 Pinguet, W. Shi, et al., 2021. OC6 Phase Ib: Validation of the CFD predictions of difference-frequency wave  
806 excitation on a FOWT semisubmersible. *Ocean Eng.* 241, 110026.  
807 <https://doi.org/10.1016/j.oceaneng.2021.110026>.
- 808 [13] I. Bayati, J. Jonkman, A. Robertson, A. Platt, 2014. The effects of second-order hydrodynamics on a  
809 semisubmersible floating offshore wind turbine. *J. Phys.: Conf. Ser.* 524(1), 012094.  
810 <https://doi.org/10.1088/1742-6596/524/1/012094>.
- 811 [14] F. Lemmer, W. Yu, P.W. Cheng, A. Pegalajar-Jurado, M. Borg, R.F. Mikkelsen, H. Bredmose, The Triplespar  
812 campaign: Validation of a reduced-order simulation model for floating wind turbines. In: *ASME 37th*  
813 *International Conference on Ocean, Offshore and Arctic Engineering*; 2018.  
814 <https://doi.org/10.1115/OMAE2018-78119>.
- 815 [15] M.I. Kvittem, P.A. Berthelsen, L. Eliassen, M. Thys, Calibration of hydrodynamic coefficients for a semi-  
816 submersible 10 MW wind turbine. In: *ASME 37th International Conference on Ocean, Offshore and Arctic*  
817 *Engineering*; 2018. <https://doi.org/10.1115/OMAE2018-77826>.
- 818 [16] P.A. Berthelsen, R. Baarholm, C. Pákozdi, C.T. Stansberg, A. Hassan, M. Downie, A. Incecik, Viscous drift  
819 forces and responses on a semisubmersible platform in high waves. In: *ASME 28th International Conference on*  
820 *Ocean, Offshore and Arctic Engineering*; 2009. <https://doi.org/10.1115/OMAE2009-79483>.
- 821 [17] P.A. Berthelsen, E.E. Bachynski, M. Karimirad, M. Thys, Real-time hybrid model tests of a braceless semi-  
822 submersible wind turbine: Part III – Calibration of a numerical model. In: *ASME 35th International Conference*  
823 *on Ocean, Offshore and Arctic Engineering*; 2016. <https://doi.org/10.1115/OMAE2016-54640>.
- 824 [18] M. Böhm, A. Robertson, C. Hübler, R. Rolfes, P. Schaumann, 2020. Optimization-based calibration of  
825 hydrodynamic drag coefficients for a semisubmersible platform using experimental data of an irregular sea  
826 state. *J. Phys.: Conf. Ser.* 1669, 012023. <https://doi.org/10.1088/1742-6596/1669/1/012023>.
- 827 [19] A.N. Simos, F. Ruggeri, R.A. Watai, A. Souto-Iglesias, C. Lopez-Pavon, Slow-drift of a floating wind turbine:  
828 An assessment of frequency-domain methods based on model tests, *Renew. Energy* 116 (2018) 133–154.  
829 <https://doi.org/https://doi.org/10.1016/j.renene.2017.09.059>.
- 830 [20] A. Pegalajar-Jurado, H. Bredmose, Reproduction of slow-drift motions of a floating wind turbine using second-  
831 order hydrodynamics and Operational Modal Analysis, *Mar. Struct.* 66 (2019) 178–196.  
832 <https://doi.org/10.1016/j.marstruc.2019.02.008>.
- 833 [21] H. Li, E.E. Bachynski-Polić, 2021. Analysis of difference-frequency wave loads and quadratic transfer  
834 functions on a restrained semi-submersible floating wind turbine. *Ocean Eng.* 232, 109165.  
835 <https://doi.org/10.1016/j.oceaneng.2021.109165>.

- 836 [22] H. Li, E.E. Bachynski-Polić, 2021. Validation and application of nonlinear hydrodynamics from CFD in an  
837 engineering model of a semi-submersible floating wind turbine, *Mar. Struct.* 79, 103054.  
838 <https://doi.org/10.1016/j.marstruc.2021.103054>.
- 839 [23] A.N. Robertson, E.E. Bachynski, S. Gueydon, F. Wendt, P. Schünemann, J. Jonkman, Assessment of  
840 experimental uncertainty for a floating wind semisubmersible under hydrodynamic loading. In: *ASME 37th*  
841 *International Conference on Ocean, Offshore and Arctic Engineering*; 2018.  
842 <https://doi.org/10.1115/OMAEE2018-77703>.
- 843 [24] C.-H. Lee, *WAMIT Theory Manual*, Massachusetts Institute of Technology, Department of Ocean Engineering,  
844 Cambridge, Massachusetts, USA, 1995. <http://wamit.com/Publications/tmanual.pdf> (accessed 23 July 2021).
- 845 [25] W. Cummins, *The impulse response function and ship motion*, David Taylor Model Basin, Washington, D.C.,  
846 USA, 1962.
- 847 [26] J. Jonkman, A. Robertson, G. Hayman, *HydroDyn User's Guide and Theory Manual*, National Renewable  
848 Energy Laboratory, Golden, Colorado, USA, 2014.
- 849 [27] S. Gueydon, T., Duarte, J. Jonkman, Comparison of second-order loads on a semisubmersible floating wind  
850 turbine. In: *ASME 33<sup>rd</sup> International Conference on Ocean, Offshore and Arctic Engineering*; 2014.  
851 <https://doi.org/10.1115/OMAEE2014-23398>.
- 852 [28] S. Zhang, T. Ishihara, Numerical study of hydrodynamic coefficients of multiple heave plates by large eddy  
853 simulations with volume of fluid method, *Ocean Eng.* 163 (2018) 583–598.  
854 <https://doi.org/10.1016/j.oceaneng.2018.03.060>.
- 855 [29] H. Li, E.E. Bachynski, Experimental and numerical investigation of nonlinear diffraction wave loads on a semi-  
856 submersible wind turbine, *Renew. Energy* 171 (2021) 709–727. <https://doi.org/10.1016/j.renene.2021.02.152>.
- 857 [30] J.R. Chaplin, P. Teigen, Steady flow past a vertical surface-piercing circular cylinder, *J. Fluids Struct.* 18(3–4)  
858 (2003) 271–285. <https://doi.org/10.1016/j.jfluidstructs.2003.07.009>.
- 859 [31] C. Clement, *Investigation of floating offshore wind turbine hydrodynamics with computational fluid dynamics*.  
860 Doctoral dissertation. University of Rouen Normandy, France, 2021.
- 861 [32] F. Lemmer, W. Yu, P.W. Cheng, 2018. Iterative frequency-domain response of floating offshore wind turbines  
862 with parametric drag. *J. Mar. Sci. Eng.* 6(4), 118. <https://doi.org/10.3390/jmse6040118>.
- 863 [33] A.D. Boon, *Drag of a surface piercing cylinder in fast current and low waves*. Master's thesis. Delft University  
864 of Technology, Netherlands, 2020.
- 865 [34] H. Li, E.E. Bachynski-Polić, 2021. Experimental and numerically obtained low-frequency radiation  
866 characteristics of the OC5-DeepCwind semisubmersible. *Ocean Eng.* 232, 109130.  
867 <https://doi.org/10.1016/j.oceaneng.2021.109130>.
- 868 [35] L. Wang, R.W. Yeung, An efficient hybrid integral-equation method for point-absorber wave energy converters  
869 with a vertical axis of symmetry, *Appl. Ocean Res.* 86 (2019) 195–206.  
870 <https://doi.org/10.1016/j.apor.2019.02.010>.
- 871 [36] D. Son, V. Belissen, R.W. Yeung, Performance validation and optimization of a dual coaxial-cylinder ocean-  
872 wave energy extractor, *Renew. Energy* 92 (2016) 192–201. <https://doi.org/10.1016/j.renene.2016.01.032>.